Tahir *et al. Biochar* (2026) 8:31
https://doi.org/10.1007/s42773-025-00539-y

Biochar

ORIGINAL RESEARCH Open Access

Engineering the microbial-electrochemical interface: synergistic of co-fe nano biochar composites for enhanced electron channelling to alter the metabolic pathway in light-driven biohydrogen production

Nadeem Tahir[1†], Hina Ramzan[1*†], Faiqa Nadeem[1], Muhammad Usman[1], Muhammad Shahzaib[1], Muneeb Ur Rahman[1], Yang Liu[2], Waheed Afzal[3], Su Shiung Lam[6,7] and Zhiping Zhang[1,4,5*]

Abstract

Photofermentative biohydrogen production (PFHP) is a promising route for sustainable biohydrogen production, but its efficiency is constrained by inefficient intra/extracellular electron transfer (IET/EET). Biochar (BC) provides unique characteristics to enhance IET/EET in biochemical systems; however, non-conductive polymer groups hinder its charge transfer efficiency. The present study proposes the engineering of the microbial-electrochemical interface through dual metal (Co and Fe) functionalization of BC to improve charge transfer within the fermentative medium, thus leading to an increase in hydrogen production. SEM, BET, XPS, and Raman spectroscopy demonstrated that Co-Fe/BC functionalization results in 22.83% higher porosity and surface area compared to pristine biochar (PBC) and single metal functionalization, suggesting increased electrons from surface defects like oxygen vacancies (OVs). The optimal loading concentration (20 mg/L) of Co-Fe/BC enhanced the biohydrogen production rate and yield by 101.61% and 103.11%, respectively, exceeding the control group (CG). Electrochemical studies showed that the lowest interfacial charge transfer resistance (1.74 Ω, 1.22 mA redox current) in Co-Fe/BC increases charge transfer capabilities by 106.77% compared to PBC (4.66 Ω, 0.59 mA redox current) thus serving as an electron shuttle to increase redox sites through flavin and c-cytochrome. IET/EET enhancement in a bioreactor loaded with Co-Fe/BC regulates butyric acid to acetic acid metabolism, as revealed by microbial community analysis, where Clostridium was 86.72% more prevalent than CG (79.77%). This work demonstrates that Co-Fe functionalized BC not only bridges electron transfer bottlenecks but also provides a conductive interface for sustained microbial-electrochemical interactions, offering a scalable strategy for optimizing renewable biohydrogen production.

[†]Nadeem Tahir and Hina Ramzan have equally contributed to this work.

*Correspondence:
Hina Ramzan
hina.ramzan91@yahoo.com
Zhiping Zhang
zhangzhiping715@163.com
Full list of author information is available at the end of the article

Springer

Highlights

- Co-Fe/BC exhibited a higher SSA, providing more active sites, and shifting the redox cycle Fe3+ to Co2+ creates OVs.
- Co-Fe/BC incorporation increased the H_2 yield through enhanced metabolic rate via electron-conducting channels.
- The loading of Co-Fe/BC changed the metabolic pathway from BA to AA, with Clostridium being the most abundant genus.

Keywords Agricultural waste, Biochar, Electron transfer, Surface functionalization, Biohydrogen

Graphical Abstract

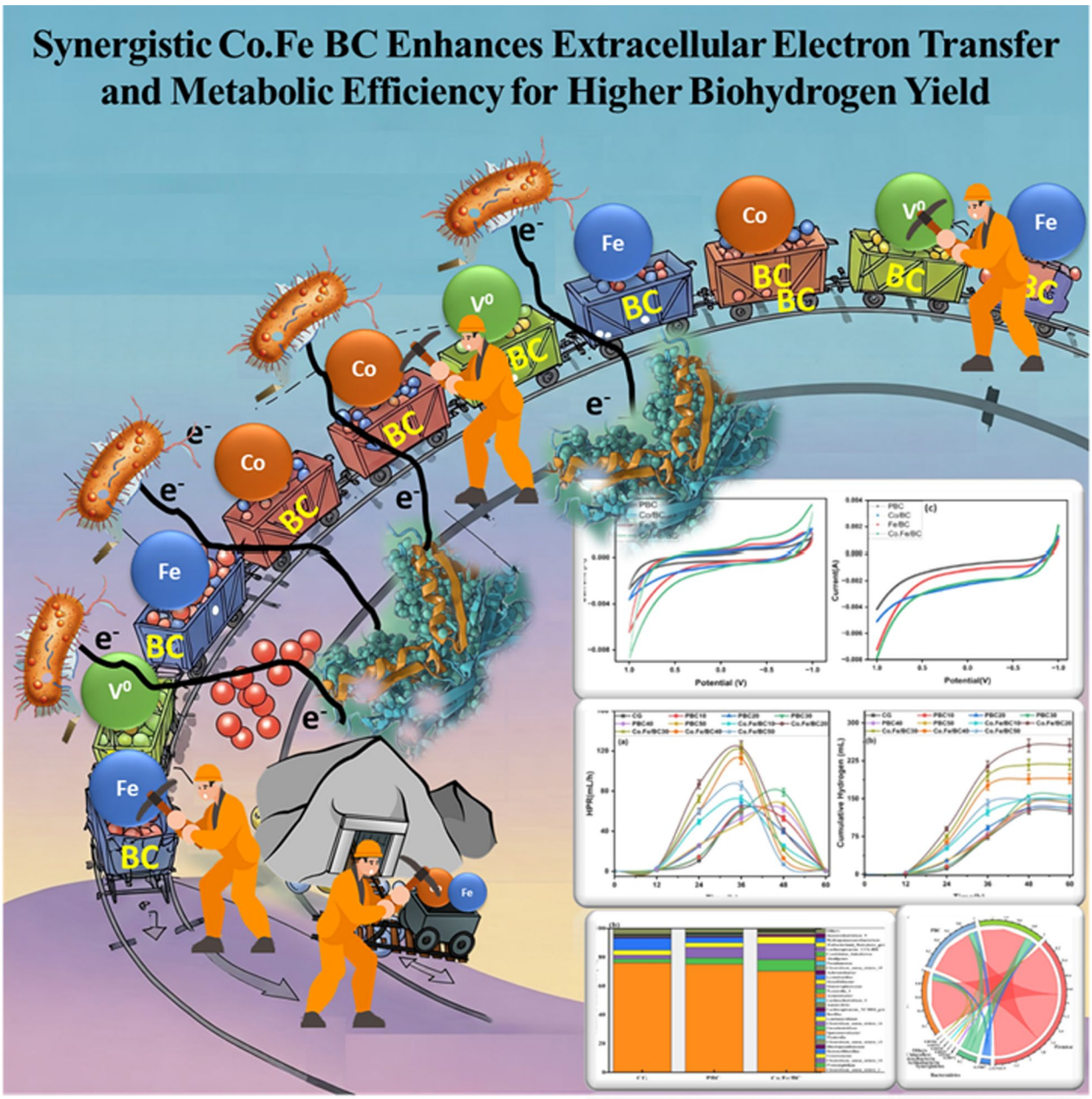

1 Introduction

The escalating global energy demand, projected to rise significantly in the coming decades, underscores the urgent need to explore and develop efficient methods for harnessing the vast potential of this resource. Furthermore, the imperative to reduce our reliance on finite fossil fuel reserves and mitigate the detrimental environmental consequences, including the alarming increase in greenhouse gas emissions, necessitates the development of innovative and sustainable energy conversion technologies (Ramzan et al. 2019; Ramzan et al. 2023). Hydrogen energy has been the focus of research due to its attractive characteristics, such as high energy density (122 kJ/g) compared to conventional hydrocarbons, and the sustainable supply of green energy as its by-product, which is only water when burned, leading to net-zero carbon emissions. Among the available various routes of biohydrogen production, the PFHP is known to be more attractive due to its several advantages, including fewer energy requirements, utilization of solar energy, operational simplicity, ability to utilize a variety of organic substrates, including abundant agricultural wastes (Roychowdhury And Ghosh 2024), and being environmentally safe. Despite the availability of abundant lignocellulosic biomass, its efficient conversion into biohydrogen is hindered by its complex and recalcitrant structure. Various techniques have been developed to alter traditional photo fermentation processes to increase biohydrogen production, including genetically modifying H_2-producing bacteria (Tiang et al. 2020), improving pre-treatment (Suriyachai et al. 2020), optimizing the bioreactor/bioprocess, adding metabolic enhancers like metal additives (Usman et al. 2024), adding inorganic/organic nanoparticles (Nadeem et al. 2020), incorporating BC or activated carbon, and carbon nanocomposites etc. (Ramzan et al. 2024; Usman et al. 2025). Among materials based on carbon composites, graphene-supported iron composites have demonstrated significant potential in boosting biohydrogen production. The magnetite/graphene oxide nanocomposite generated 112.4 mL of H_2 during dark fermentation, due to its excellent electron conductivity and ability to stimulate microbes. However, these benefits often come with challenges such as complex synthesis methods, high costs, and additional functionalization requirements to promote microbial activity compatibility (Table S1) (Mostafa et al. 2016). However, in comparison to carbon-based materials, the application of nano BC has emerged as a promising pathway of nanotechnology that holds significant potential to enhance the efficiency of lignocellulosic biomass conversion through enhanced redox reactions and electron transfer efficiency, resulting in a 69.2–220% rise in the bioelectrochemical system's current density, which boosts bacteria's electron shuttling to accelerate EET and encourages the oxidation of volatile fatty acids (VFAs) (Kayoumu et al. 2025). Additionally, corn straw, a vital agricultural solid waste, has a consistent yearly production of 310 million tons in China and 1 billion tons worldwide. The burning and direct disposal of a large amount of corn straw as solid waste leads to resource waste and air pollution. Corn straw's huge production, high cellulose and hemicellulose content make it perfect for synthesizing porous BC (Zeng et al. 2024). Corn straw biochar outperforms graphene and other composites by offering superior cost efficiency and enhanced biocompatibility, which promote microbial adhesion and its modification enhances electron transfer in biohydrogen production. Additionally, it provides a sustainable, hierarchical porous structure that facilitates higher metal loading and microbial colonization compared to other carbon-based materials (Ma et al. 2019). The BC amendment led to a 317.1% increase in biohydrogen production in a dark fermentation system by stimulating bacterial growth and doubling the electron transfer efficiency compared to CG (Bu et al. 2021). The addition of BC not only increases the biohydrogen production through redox active sites and surface functionalities but also functions as an Exogenous Electron Mediator (EEMs) facilitating electron transfer within the microbial system (Yu et al. 2025). Furthermore, its inherent novel characteristics, such as high specific surface area (SSA) offer more sites for microbes to grow and facilitate the adsorption of the substrate, and its porous structure could promote microbial colonization and growth potential (Wang et al. 2025), BC contains buffering groups like carbonates, trace element richness, and amino acids, which can regulate pH and reduce the lag phase. On the other hand, the surface of BC contains functional groups with a negative charge, which limits the catalytic ability and weakens the electron transfer capacity (ETC). Thus, altering the ETC of pristine BC through the degree of graphitization and modification through surface functionalization with external metals can enhance the charge transfer through conductive bridges, electron mobility, and thus strengthen conductivity (Xiao et al. 2022; Wang et al. 2023a).

Among other metals, iron (Fe) and cobalt (Co) are non-noble transition metals that are well-known for their catalytic activity across a wide range of chemical and biological processes. Their relative abundance and lower cost compared to noble metals like platinum make them particularly attractive for large-scale applications in energy production. Fe has been claimed to be a conductive medium, create an e^- transport system with methanogens, and facilitate e^- flow between microorganisms and external e^- carriers like NADH (Engliman et al. 2017). The surface properties of BC are altered by the addition

of iron in various forms, including iron salts, iron oxides, or nano-zero-valent iron, which can impact the functional groups, pore size, surface charge, and surface area (Reddy et al. 2017). The Fe-modified BC promotes the habitat and metabolism of exoelectrogens, featuring a highly accessible SSA of 10.141 m^2/g and a porous structure (Ratheesh et al. 2024). Nevertheless, the actual application of Fe-loaded BC remains challenging due to the constraints of acidic conditions and the loss of active sites resulting from Fe leaching or low stability. The interaction force between a single metal and biochar in Fe-BC is weak, which causes leaching and reduces the efficiency of the Fe-BC. Compared to a single metal catalyst, bimetallic doping has extremely high chemical stability and synergistic effects due to the Co_7Fe_3 alloy (Liu et al. 2024). It has been reported that the supplementation of Co-based compounds can significantly enhance the biohydrogen production, accelerating electron transfer, boosting the hydrogenase activity of the PF system. Their magnetization optimizes enzyme kinetics and extracellular electron transport by altering stretching vibrations of proteins, co-enzymes energy levels, and reducing activation losses as the Lorentz force generated by the magnetic field lowers the activation and ohmic losses of biological systems (Suriyachai et al. 2020). The absence of cobalt may result in the accumulation of organic acids and a rapid decrease in pH, which likely limits microbial activity (Zhu et al. 2025). Recently several studies have explored the synergy of bimetallic (Fe/Co) based biochar however their applications have been restricted to the activation of persulfate and peroxymonosulfate to remove contaminations (Liu et al. 2024; Hao et al. 2022; Wang and Wang 2023). Based on recent results, functionalized BC with Co^{2+} and Fe^{3+} may lead to a significant synergistic effect that not only provides the charge transferring channels but also maintains the exceptional properties of BC, facilitating electron transfer between microorganisms and enhancing the metabolism of the fermentative system. The present study deals with the engineering of a microbial-electrochemical interface with a light-responsive Co-Fe-biochar composite to act as an electron sink, altering its metabolic pathways and its application to directly manipulate microbial metabolism in photofermentation remains unexplored.

Thus, the objective of this present work was to alter the intrinsic ETC of the nano-BC through its surface functionalization with dual metals (Co and Fe) and to study its effect on IET/EET in PFHP from corn stover (CS) lignocellulosic biomass. The physicochemical characteristics such as morphology and crystallinity, SSA and pore size, and electronic configuration of the surface atoms of the PBC, and surface functionalized Co/BC, Fe/BC, and Co-Fe/BC were investigated by scanning electron microscope (SEM), Brunauer–Emmett–Teller (BET), and X-ray photoemission spectroscopy (XPS) techniques, respectively. Moreover, the electronic configuration and surface functional groups were investigated using Raman spectroscopy and FTIR spectroscopy, respectively. The capability of the bacteria to perform EET was evaluated using CV, DPV, linear sweep voltammetry (LSV), chronoamperometry (CA), and electrochemical impedance spectroscopy (EIS). Eventually, the effects of metal-functionalized BC on H_2 production rate, H_2 yield, reducing sugar, metabolites, pH, oxidation–reduction potential (ORP), and microbial community analysis were investigated in detail.

2 Materials and methods

2.1 Synthesis of BC

As one of the most abundant agricultural wastes worldwide, CS offers a sustainable, cost-effective, and environmentally friendly feedstock, rich in cellulose (34.63%) and hemicellulose (26.56%), suitable for biochemical conversion (Nadeem et al. 2020), making it a sustainable and economically favorable feedstock for PFHP and substrate for catalyst synthesis. The agricultural residue-based lignocellulosic biomass of CS was collected from a nearby farm in Henan Province, China. After being washed and dried at room temperature, the samples were pulverized using a herb grinder from Baixin Machinery Factory, Ruian, China (Tahir et al. 2021). The CS sample was then put into a cleaned porcelain crucible and pyrolyzed at a heating rate of 10 °C/min for 2 h at 900 °C in a muffle furnace under oxygen-limited conditions. After being cooled to room temperature, the BC was removed, stored at room temperature, and labelled as PBC. For Fe and Co-functionalized BC fabrication, 20 g of crushed CS was mixed well with 100 mL of 10% $Fe(NO_3)_3.9H_2O$ and $Co(NO_3)_2.6H_2O$ for 4 h with uniform stirring. Later on, the solution was filtered and dried in an oven for 12 h at 80℃. The mixture was pyrolyzed under the same pyrolysis conditions used for PBC synthesis, and the resulting materials were named Co/BC and Fe/BC. For the co-functionalization of metals on BC, 5% of each metal salt was mixed thoroughly, synthesized under previously used pyrolysis conditions, and after cooling, the Co-Fe/BC was removed and stored at ambient temperature (Liu et al. 2023a).

2.2 Investigating the physio-chemical and optical characteristics of BC

The morphology of the synthesized BC was examined using scanning electron microscopy (SEM, ZEISS Gemini 300) at an accelerating voltage of 3 kV (Zhang et al. 2023). To study the crystallinity structure of the studied BCs, an X-ray diffractometer (Bruker D8 Advance, D/MAX-2000)

was used at 40 kV and 30 mA with Cu-Kα radiation (λ = 1.5406 Å) at a scan rate of 10°/min with a step size of 0.04°. BET-SSA, along with BJH pore size analysis, was analyzed using a MicrotracBEL (BELSORP-mini II) (Liu et al. 2023a). XPS was conducted using a Thermo Scientific K-Alpha spectrometer, which is equipped with 300W Al-Kα radiation, to identify the elemental chemical state on the BC surface (Rahman et al. 2024). Raman spectroscopy (LabRam HR Evolution, HORIBA) was performed at a wavelength of 532 nm, using a laser in backscattering geometry at room temperature. This method aimed to identify the amorphous and graphite phases of the samples, employing a 50 × objective across a range of 200–1800 cm^{-1} with an integration time of 0.5 s, whereas a Bruker Vertex 80 V was used to perform FTIR measurements.

2.3 Electrochemical analysis of BC

On a CHI760E electrochemical workstation, electrochemical measurements of PBC, Co/BC, Fe/BC, and Co-Fe/BC tests were conducted using a three-electrode system comprising a working electrode constructed from FTO (fluorine-doped tin oxide) with synthetic catalysts, a reference electrode of Ag/AgCl, and a counter electrode made of Pt. To ensure the consistency and facilitate the comparison with literature, all electrode potentials recorded versus Ag/AgCl were converted to the reversible hydrogen electrode (RHE) scale using the following Eq. 1:

$$ERHE = EAg/AgCl + 0.059 \times pH + 0.197 \quad (1)$$

Here, 0.197 represents the standard potential of the Ag/AgCl reference electrode, and pH refers to the electrolyte measured pH of 7. During the electrochemical study, a 0.1 M Na_2SO_4 solution with a pH of 7 was used as the electrolyte. The 1 cm × 1 cm FTO plates were used to create a thin film of the substrate, which was then washed thoroughly with distilled water, isopropyl alcohol, and acetone, and dried at 100 °C in an air oven. After adding 20 mg of each BC individually to 40 mL of acetone and sonicating for 10 min, working electrodes were made using the drop-casting technique (Rahman et al. 2024). The CV measurements were performed (−1 to 1 V) with a scanning rate of 0.05 mV/s, and the BC's redox behavior was compared to that of the simple FTO electrode. An AC signal with an amplitude of 10 mV and a frequency range of 1–10 MHz was used to obtain the EIS spectrum. To investigate the impact of BC on extracellular electroactive secretions, a DPV test was conducted using a three-electrode system with the following parameters: pulse width of 0.05 s, potential increment of 5 mV, quiet time of 2 s, potential scan range from 0 to -0.9 V, and amplitude of 10 mV. Using CA, the BC's electron-donating (EDC) and electron-accepting (EAC) capacities were ascertained. To determine the zeta potential of BC, a 150 mL conical flask containing 0.02 g of samples was filled with 50 mL of distilled water, and the pH of the suspension was adjusted with HCl or NaOH to bring it between 6 and 7. The suspensions were then ultrasonically dispersed in a sonicator at a frequency of 40 kHz and a power of 300 W for 30 min at 25 °C. The zeta potential of the BCs was then determined using a Nanotrac Wave II (Microtrac, USA) (Rahman et al. 2024; Rahman et al. 2025).

2.4 Preparation of microbial growth media

In this investigation, the Laboratory of Nano-photocatalytic Materials at Henan Agricultural University provided the purple non-sulfur bacteria (PNSB) *Rhodopseudomonas palustris.* The PNSB bacteria were grown by preparing a medium that comprised 1.0 g/L K2HPO4, 0.5 g/L MgCl2, and 10.0 g/L yeast extract. The starting pH was adjusted to 7, and the medium was sterilized at 120 °C for 15 min (Nadeem et al. 2020; Shahzaib et al. 2024). The PNSB growth media and PNSB were mixed in 1:1 (v/v), and the cultures were grown under an incandescent light with an intensity of 192 W/m^2 at 30 ± 2 °C until their initial cell-concentration reached 875 mg/L (Tahir et al. 2022).

2.5 Batch fermentation

A glass bioreactor with a capacity of 250 mL was used for the batch experiment of biohydrogen production, and to guarantee the reliability of the experimental findings, each experiment was carried out in triplicate. The fermentation media contained, 0.4 g/L NH_4Cl, 0.2 g/L $MgCl_2$, 0.1 g/L yeast powder, 0.5 g/L K_2HPO_4, 2 g/L NaCl, 3.56 g/L sodium glutamatic acid, 14.8 g/L sodium citrate dihydrate, and 0.085 g/L citric acid monohydrate, 6 g/L CS. To see the effect of functionalized BC on PFHP, the various concentrations of studied BC such as 0, 10, 20, 30, 40 and, 50 mg/L were loaded into bioreactors, whereas the bioreactor with a loading concentration of 0 mg/L was set as CG, and the initial pH of the bioreactors was set to 7. To keep an anaerobic environment, before the experiment, nitrogen gas was used to purge all of the bioreactors for five minutes and they were carefully wrapped with rubber plugs and incubated at 30 °C under 190 W/m^2 using an incandescent lamp.

2.6 Analytical methods

The gas produced during the fermentative process was sampled every 12 h, and biohydrogen concentration was analyzed through gas chromatography (GC112N, INESA, China) with N_2-gas as a carrier with 40 mL/min flow rate, whereas the temperature of the column, intake, and

thermal conductivity detector was at 100 °C, 150 °C, and 150℃, respectively. To investigate the VFAs in the fermentation broth (sampled after every 12 h), a gas chromatograph (Agilent 6890B) was used with a gas carrier with 30 mL/min argon gas flow, a flame ionized detector, and the syringe temperature was controlled at 250 °C, and the detector temperature controlled at 300 °C, respectively. A pH meter (PHS-3C, Youke, China) was used to measure the pH of the fermentation broth. Utilizing the DNS technique and a UV–Vis spectrophotometer (T2602, YOUKE, China) at an optical density of 540 nm, the variations in RS during the biohydrogen production batch experiment were examined (Liu et al. 2023b). The number and geographical distribution of microorganisms in the CG and BC treated groups were investigated using high-throughput sequencing. The 16S rRNA gene was pyrosequenced at high throughput to yield microbiological communities. The DNA quantity was measured using the (Omega-soil DNA) reagent produced by Omega Bio-Tek in Norcross, USA, described in our earlier work (Tahir et al. 2022). In the present study, the modeling of biohydrogen production was based on two kinetic models, the Gompertz and Monod models. A modified Gompertz model was used to examine the highest PFHP potential to determine the kinetic parameters, which are provided in Eq. 2

$$H(t) = P \times exp\left\{-\exp\left[R_{max} \times \frac{E(x-t)}{P+1}\right]\right\} \quad (2)$$

H(t) represents the cumulative H_2, P the highest possible H_2 yield (mL), (R_{max}) the maximum HPR (mL/h), x the lag phase in hours, (t) the incubation period, and the Euler number is constant (E = 2.71828).

The growth kinetic model was described using the Monod kinetics equation, which relies on the concentration of a single substrate. The equation is predicated on the correlation between the rate of cell growth and the concentration of substrate. It may be defined by the Monod equation as 3:

$$\mu = \frac{(\mu_{max} S)}{(Ks + S)} \quad (3)$$

μ_{max} represents the maximum specific growth rate (h^{-1}), while K_s is the Monod saturation coefficient for cell growth expressed in g/L. The value of K_s aligns with the substrate concentration (S) measured in g/L when μ equals 0.5 μ_{max}.

3 Results and discussion

3.1 Physio-chemical characteristics of BCs

The morphology of the PBC and the surface-functionalized BC, as studied by SEM, is shown in Fig. 1(a, b). The raw material of CS has a size in the range of microns with irregular shapes having clear surface roughness, Fig. 1S(a). Before functionalization, the surface of PBC was quite scaly, and the irregular pore structure was readily apparent. Based on the SEM image shown in Fig. 1(a), it is evident that the PBC has a crystalline mesoporous surface structure. After functionalization, the BC surface was relatively smooth with many irregular tiny particles attached, which should be magnetic Fe and Co under high-temperature functionalization of metals during pyrolysis, Fig. 1(b) (Hamid et al. 2022). The C, O, and S atomic content of PBC reached 84.27%, 15.54%, and 0.17%, respectively, Fig. 1S(b), while Co-Fe/BC atomic composition of C, N, O, S, Fe, and Co were 71.83%, 0.17%, 21.53%, 0.23%, 3.49%, and 2.74%, respectively Fig. 1S(c).

The crystallinity structure of CG, PBC, and metal-functionalized BC (Co/BC, Fe/BC, and Co-Fe/BC) is shown in Fig. 1(d). Two significant peaks in all BC and CG can be seen in the region of 2θ = 22–23° and 40–45°, which correspond to amorphous carbon (002) and graphite structure (100) planes, respectively. In PBC, the experimental findings are in good agreement with the literature where an intense sharp peak around 2θ = 26–28° (96-900-6292) may corresponds to Si sediment presence in biomass samples during the grinding process or XRD substrate (Yi et al. 2020). It is observed that the observed XRD peak at 2θ = 31.95°, 32.19°, 62.97°, and 79.65°, in Fe/BC are characteristic peaks of Fe_2O_3 and are related to (220), (222), (311), and (111) crystal planes, respectively (JCPD Card 96-222-7903). The characteristic diffraction peaks observed at 59.22° and 65.10° are correlated to the (422) and (440) crystalline planes of Fe_3O_4 (Lin et al. 2024). The XRD diffraction peaks might imply that the Fe_3O_4 and Fe_2O_3 particles were successfully deposited on the BC. The lattice parameters for Fe/BC are a = 9.05 Å, b = 9.15 Å, c = 11.32 Å, and Fe^{2+} and Fe^{3+} have ionic radii of 0.78 Å and 0.64 Å. For Co-BC, a substantial peak was observed at 43.6°, signifying the structure of CoCx (JSPDS, 44–0962). Co^{2+} and Co^{3+} have ionic radii of 0.74 Å and 0.61 Å and have lattice parameters of a = 8.65 Å, b = 11.70 Å, c = 8.30 Å (JCPD card 96–700-2861). The change in lattice parameters is due to the larger ionic radii of Fe than Co. When Co^{2+} replaces Fe^{2+} in the lattice site, the overall lattice parameter slightly decreases. Co-Fe/BC revealed sharp and narrow diffraction peaks around 45°, which correspond to the Co-Fe alloy formation (Wang et al. 2023b; Sun et al. 2025), which is beneficial for improved catalytic activity (JCPD Card 44–1433) respectively. Liu et al. also found the same phenomenon during the research of Fe-Co@N-BC (Wang and Wang 2023). The conversion of Fe^{3+} to Fe^{2+} was significantly facilitated by the redox cycle between

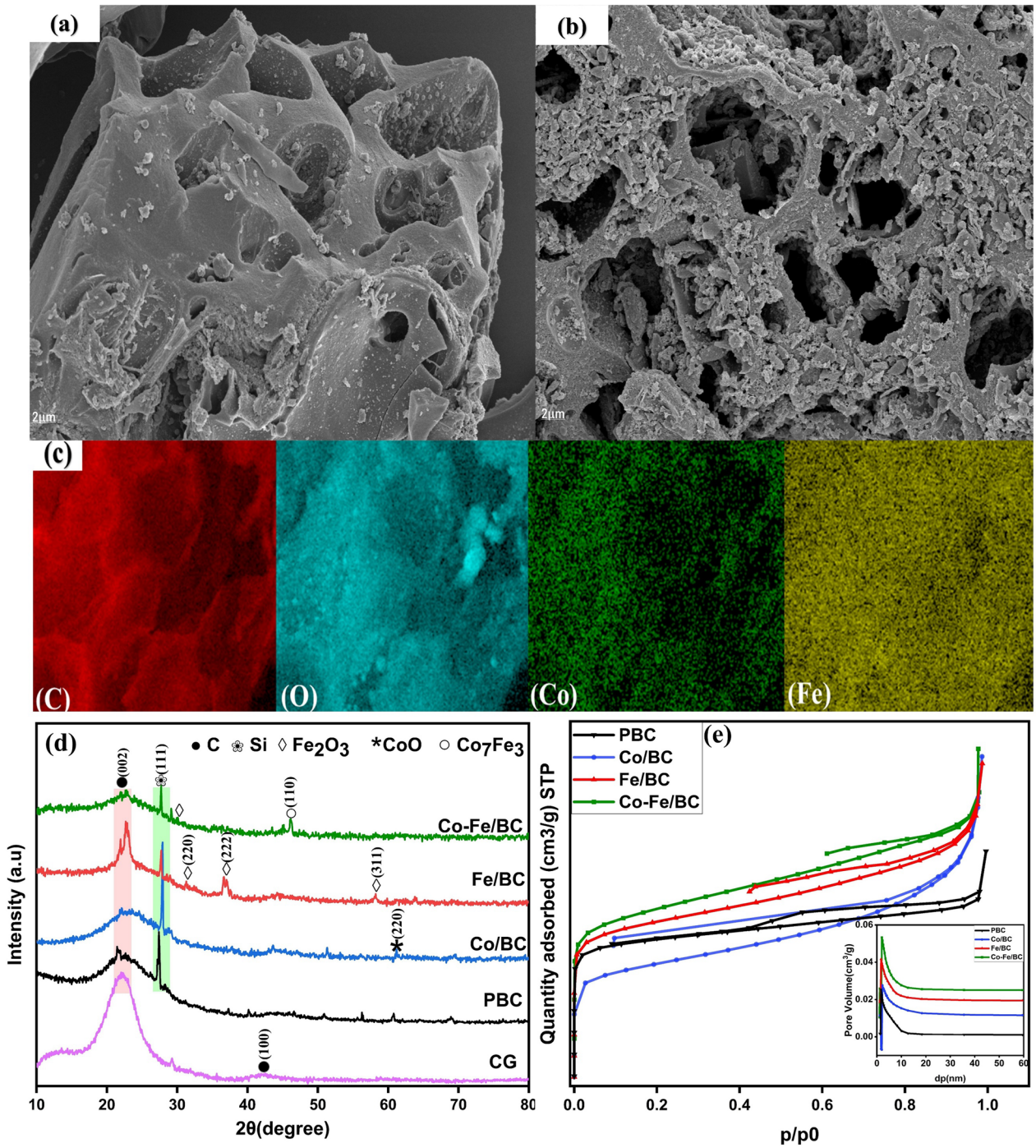

Fig. 1 SEM images of **a** PBC **b** Co-Fe functionalized BC **c** Elemental mapping of Co-Fe/BC **d** XRD analysis of BC **e** BET and BJH analysis of PBC and functionalized BC

Co^{2+} and Co^{3+}, which resolved the issue of Fe^{2+} regeneration difficulty. Meanwhile, the plentiful OVs produced by the redox within Co-Fe bimetal considerably improved catalytic performance. Furthermore, the observed XRD peaks in Co-Fe/BC ($2\theta = 19–30°$ and $2\theta = 40–50°$) are sharper in functionalized BC as compared to the PBC, which suggests that dual metal functionalized BC has turbostratic carbon crystallite formation while others show more graphite-like structure (Guo et al. 2023a). The Fe/BC and Co/BC higher intensity peaks were slightly

Table 1 BET SSA, BJH meso, and micropore analysis of PBC and Co-Fe functionalized BC

Sample	BET-SSA (m^2/g)	Mesopore volume (cm^3/g)	Mesopore diameter (nm)	Micropore volume (cm^3/g)	Micropore diameter (nm)	t-plot SSA (m^2g^{-1})
PBC	308.06	0.134	7.695	–	–	–
Co/BC	320.92	0.171	6.449	0.117	1.085	413.33
Fe/BC	354.32	0.184	3.942	0.148	1.348	443.38
Co-Fe/BC	378.40	0.197	3.580	0.209	1.612	471.23

shifted and broadened in the co-functionalized Co-Fe/BC; this was explained by variations in the size of the crystals and the crystal structure's capacity to expand or compress.

The nitrogen adsorption and desorption measurements were employed to examine the effect of Fe and Co loadings on the porosity and SSA of BC, Fig. 1(e). It can be seen that PBC belonged to a type IV hysteresis loop containing mesopores and having 308.06 m^2g^{-1} BET-SSA. The pore size distribution curves of Co/BC, Fe/BC, and Co-Fe/BC revealed that the isotherms corresponded to type I and IV hysteresis loops, resulting in micropores and mesopores. Moreover, the BET-SSA of Co-Fe/BC was 378.40 m^2g^{-1}, whereas Fe/BC and Co/BC reached 354.32 and 320.92 m^2g^{-1} after the subsequent Fe and Co loading. Co-Fe/BC has 22.83%, 17.91%, and 6.79%, higher BET-SSA than PBC, Co/BC, and Fe/BC, respectively. These results agree with the SEM results and total pore volume due to increased micropore and mesopore volume. Co/BC, Fe/BC, and Co-Fe/BC have (0.117, 0.171 cm^3/g), (0.148, 0.194 cm^3/g), and (0.209, 0.197 cm^3/g) micropore and mesopore volume, respectively (Table 1). Because of the presence of Co-Fe-containing materials on the BC's surface, the increase in surface particles increased the SSA of the functionalized BC. In order to compare PBC before and after functionalization, the average pore diameter of Co/BC, Fe/BC, and Co-Fe/BC decreased by 16.25%, 48.76%, and 53.44%, respectively, it might be due to the infiltration of Fe and Co particles into BC's internal structure, which resulted in blockage of pores or pore walls collapse, thereby narrowing the average pore diameter (An et al. 2022). The graphitization degree inversely determines porosity; consequently, the Fe/BC and Co/BC need a suitable balance between mass transfer and conductivity.

The average pore diameter of Co. Fe/BC was less than that of PBC because of the non-uniform distribution of metals on the BC surface and the partial filling of pores. Numerous mesopores occurred on the PBC, while meso and micropores on the Co-Fe/BC surface showed that they may provide significant cell immobilization sites, and the porous structure also made it easier for microbes to colonize and improved the PF process. Microorganisms preferred adhering to rough surfaces, which provided an increased SSA for cell attachment (Di et al. 2022). Thus, the micropores and mesopores on Co-Fe/BC will benefit BC catalytic active sites and are favorable for electron transfer on the catalyst surface. Moreover, the higher SSA was conducive to containing enough microorganisms for growth, thus leading to an enhanced metabolic rate.

XPS analysis was used to analyze the effects of the dual-metal functionalization on the composition of the BC surface elements, chemical states, and present functional groups. The XPS survey of the chemical states of surface elements of PBC and Co-Fe/BC (C, O, Fe, and Co) is shown in Fig. 2(a). The C1s spectra of PBC are characterized by two peaks at 284.50 eV and 286.45 eV, corresponding to C=C/C–C and C–O bindings, respectively, as seen in Fig. 2(b) (Li et al. 2020a). The three primary peak types in the C1s spectra of Co-Fe/BC are located at 284.50, 286.15, and 287.60 eV, and they correspond to C=C/C–C, C–OH/C–N, and C=O/O–C=O, respectively corroborating the results of FTIR (Fig. 2(c)). The O1s core level spectra of PBC are divided into two peaks, a 530.15 eV binding energy peak related to chemisorbed oxygen and the binding energy peak near 533.09 eV, associated with C=O/OH Fig. 2(d). The O1s spectra of Co-Fe/BC have three peaks, with the 530.80 eV binding energy corresponding to the O-Metal, the binding energy peak of 532.82 eV corresponding to the OVs in Co-Fe/BC, 531.90 eV might be related to C-O, and the 534.05 eV binding energy corresponding to the C=O/OH bond. The peak between 530–532 eV is Co/Fe–O, which is consistent with the characteristics Co/Fe–O vibrational of the FTIR, Fig. 2(e) (Simoes dos Reis, et al. 2022).

The Fe 2p spectra showed peaks corresponding to the Fe 2p3/2, Fe 2p1/2, in which Fe^{2+} is attributed to the peaks at 712.05 and 724.43 eV in the Co-Fe/BC, while the peaks at 713.19 and 726.96 are assigned to the Fe^{3+} $2p_{3/2}$, and Fe^{3+} $2p_{1/2}$ compound. The asymmetry and width of the Fe XPS peak in Co-Fe/BC might indicate that Fe exhibits several oxidation states of (Fe^{2+} and Fe^{3+}), Fig. 2(f). To maintain charge neutrality in Co-Fe/BC, the valence state of Fe^{3+} changes to Fe^{2+}, resulting in the formation of OVs, and the observed

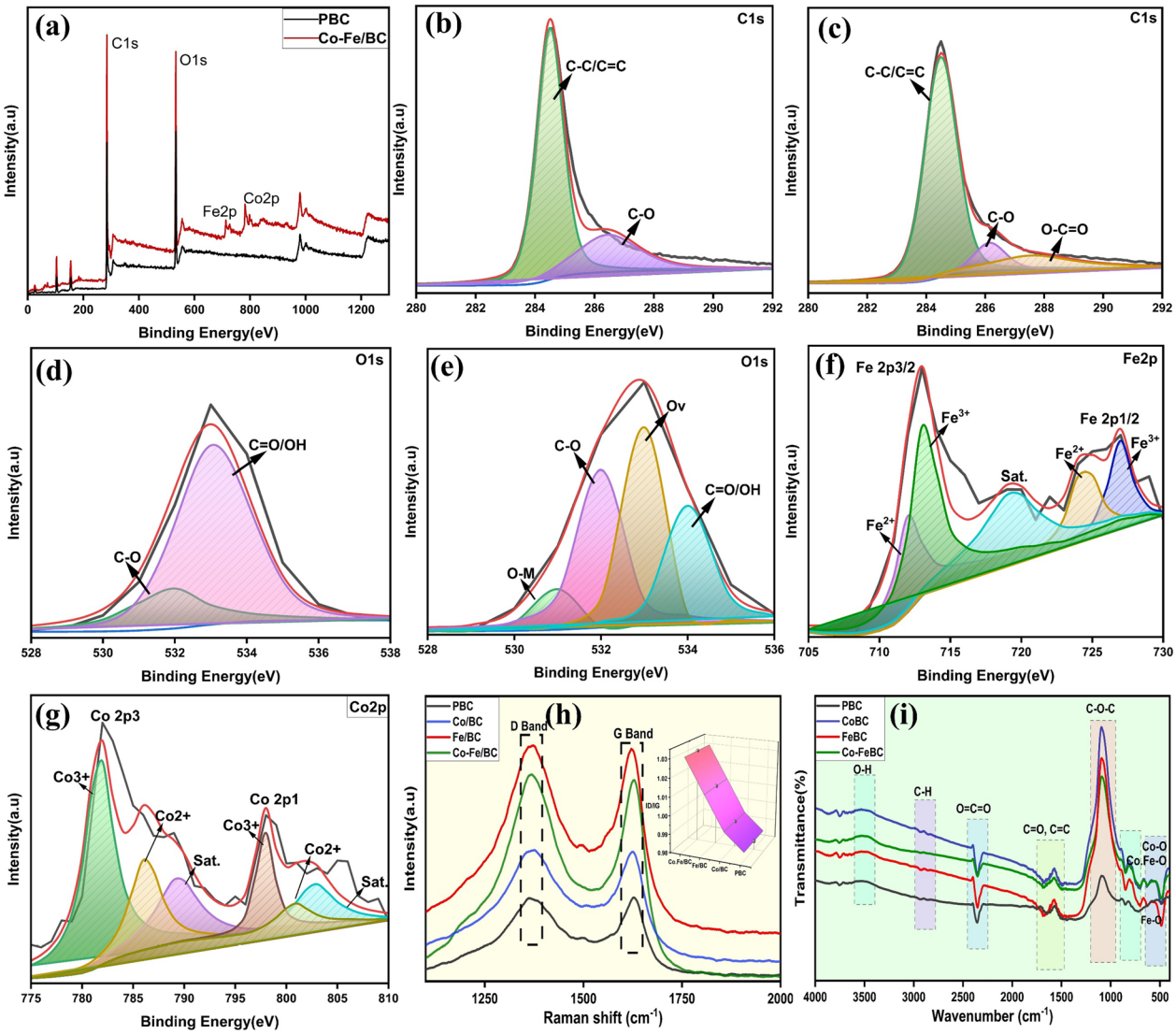

Fig. 2 XPS Study of BC **a** XPS Survey of PBC and Co-Fe/BC **b** C1s spectra of PBC **c** C1s spectra of Co-Fe/BC **d** O1s spectra of PBC **e** O1s spectra of Co-Fe/BC **f** Fe2p spectra of Co-Fe/BC **g** Co2p spectra of Co-Fe/BC **h** Raman shift and ID/IG ratio of PBC and metal functionalized BC (i) FTIR spectra of PBC and metal functionalized BC

results are in good agreement with the reported literature (Hao et al. 2022). Figure 2(g) displays the high-resolution Co2p XPS spectrum of Co-Fe/BC, providing crucial insight into the oxidation states and chemical environment of cobalt. The Co2p spectra showed peaks corresponding to Co 2p3/2 and Co 2p1/2, respectively. The peaks at 781.7 eV and 797.9 eV were attributed to Co^{3+}, while the peaks at 789.35 eV and 802.78 eV were attributed to satellite peaks of Co^{2+}. The peaks at 786.2 eV and 800.83 eV were also observed Co^{2+}; the fitting parameters are shown in the Table 2S to demonstrate fitting quality. The synergistic redox cycling between different Co oxidation states, and potentially, in conjunction with Fe, is critical for facilitating electron transfer, and the existence of these cobalt species are in good agreement with the literature (Liu et al. 2024). The redox environment in a bimetallic system like Co-Fe/BC enhances catalytic performance by providing abundant active sites for electron exchange, promoting the efficiency of EET and regulating microbial metabolism. The coexistence of Co^{2+} and Co^{3+} was observed over the functionalized BC, and the Co^{3+}/Co^{2+} redox cycle is considered advantageous for the conversion of Fe^{3+} to Fe^{2+} by resolving the regeneration of Fe^{2+} and enhancing photocatalytic activity (Sridharan et al. 2021). The analysis above indicates that the

dual-metal functionalization of Fe and Co can cause OVs generation by changing the oxidation states on the BC surface, which may enhance its catalytic activity. The role of Fe and Co in Co-Fe/BC included high specific surface area, forming pore structure, introducing magnetic components, increasing defects and providing more active sites, which cross-validates all provided results. Additionally, these defects increase charge transfer in the fermentation media, resulting in a higher metabolic rate and greater biohydrogen production (Nadeem et al. 2020).

3.2 Opto-chemical properties of BCs

Raman spectroscopy is an excellent technique for evaluating carbon materials, as it is used to determine carbon's amorphous and graphite phases (Fig. 2(h)). Two distinct peaks were found at around 1356 cm^{-1} and 1588 cm^{-1}, which correspond to the D-band and G-band, respectively. In addition, the D versus G-band (I_D/I_G) intensity ratio can speed up the electrophilic reaction to produce reactive species and improve the π-electron flow in the carbon medium by conjugation. The I_D/I_G values of PBC, Co/BC, Fe/BC, and Co-Fe/BC are 0.98, 0.99, 1.01, and 1.02, respectively, Fig. 2(h). A higher I_D/I_G ratio of Co-Fe/BC means more defects and lower graphitization, confirming that it has an amorphous structure having higher SSA than the graphitic structure, confirmed through BET investigation. With increasing Co and Fe loading in Co-Fe/BC, the samples exhibited a substantial peak current, suggesting that adding Co and Fe significantly accelerated the transfer of electrons on the Co-Fe/BC surface and reactivity (Guo et al. 2023a). This finding showed that Fe and Co functionalization can cause the carbon network to become distorted and the formation of more defects, consistent with the observed increase in oxygen containing functional groups detected by XPS and FTIR (Xu et al. 2020). Functionalization can increase the defects in the lattices of BC, which is beneficial for anchoring and dispersion of metal atoms on the surface of BC. Co/BC and Fe/BC have a higher graphitization degree than Co-Fe/BC, it can also be confirmed from BET that appropriate SSA and pore size distribution are beneficial in exposing additional reaction sites for facile catalysis interaction with substrates while retaining electrons conduction Fig. 1(e). These defect sites help the conjugated carbon system by changing its electrical charge distribution and acting as redox-active functional groups. In a similar study, Xu et al. examined the defect degree of PBC, NBCs, and Fe@N co-doped BC, and found that the Fe@N co-doped BC had more defects (Gao et al. 2022).

FTIR spectrum was performed within the range of 4000–400 cm^{-1} to determine the functionalities of BC, Fig. 2(i). The broad bands at 3450–3550 cm^{-1} may indicate the OH stretching vibration associated with hydroxyl functional groups found in alcohols, phenol, and carboxylic acid. At 2920 cm^{-1}, an aliphatic C–H stretching band is observed, indicating that the cellulose is not completely carbonized during pyrolysis. The weak peak at 2930 cm^{-1} corresponds to the alkyl group's symmetric C–H stretching, almost disappearing in Co-Fe/BC. The presence of Co and Fe reduces the activation barrier for C-H bond cleavage, promoting their decomposition. The band observed at 1725 cm^{-1} corresponds to the C=O vibration in carbonyl groups, while the band ranging from 1625–1680 cm^{-1} is attributed to C=C stretching vibration, additionally, the band at 1600 cm^{-1} is linked to quinone groups. A blue shift is noted in the peaks: PBC shows a peak around 1635 cm^{-1}, whereas Fe/BC, Co/BC, and Co-Fe/BC display peaks at 1676 cm^{-1}, 1671 cm^{-1}, and 1681 cm^{-1}, respectively, which indicates a stronger bond with the metals. The bands from 1038–1084 cm^{-1} relate to the C–O–C stretching vibration, with the most intense peak at 1077 cm^{-1} attributed to C–O, promoting the enhancement of electron transfer in functionalized BC, Fig. 2(i). This observation is strongly supported by XPS C1s analysis, where a notable increase in the relative percentage of the C–O component and the C=O was observed in Co-Fe/BC compared to PBC; furthermore, the O1s spectrum reveals distinct components for lattice oxygen and surface oxygen species (C–O/O–H), suggesting enhanced functionalization on the BC surface. It can be concluded that BC materials have a high concentration of oxygen-containing functional groups. The bands at 854 cm^{-1} and 565 cm^{-1} are attributed to Fe–OH bending vibrations and Fe–O stretching vibrations, respectively. Additionally, the bands in the range of 520–540 cm^{-1} correspond to Co–O vibrations, indicating the metal-carboxyl coordination can be confirmed from XPS results (Wang et al. 2020).

These mixed-metal complexes can alter the electronic environment around the oxygen atoms, potentially leading to less distinct C-O bond stretching (Rahman et al. 2021). The interactions between the two different metal ions and the oxygen-containing groups might not be as strong or specific as the interactions with a single type of metal ion, leading to reduced intensity of the C–O stretching vibration. Wu et al., concluded that magnetic BC displayed the distinctive Fe–O peak appears at 574.7 cm^{-1}, in contrast, the most prominent intensity peaks are located at 1020.1 cm^{-1} and 3417 cm^{-1}, corresponding to O–H and C–O stretching vibrations, which facilitate electron transfer (Wu et al. 2024).

3.3 Electrochemical characteristics of BCs

Conventional carbonaceous materials have anion exchange sites for photo-fermentative biohydrogen production. Zeta potential is a useful surface property for measuring material surface charge and stability. PBC is a material with a negatively charged surface and a low zeta potential, signifying a substantial concentration of bioactive compounds (Simoes dos Reis, et al. 2022), due to this, its surface has electrostatic repulsion to anions. To increase the anion exchange site for surface charges, the surface chemistry of BC was modified by dual metal functionalization. The shifting towards positive zeta potential for Co/BC, Fe/BC, and Co-Fe/BC validates the effective deposition of Co and Fe on the BC surface and demonstrates that metal functionalization affects the BC surface charges and can enhance electron transfer Fig. 3(a) (Hosny et al. 2022). The combination of metal functionalization may improve SSA and the dispersion of exposed iron and cobalt sites by a comprehensive mix of functionalized Fe^{3+} and Co^{2+}, which tends to move the zeta potential toward positive. The positive zeta potential in Co-Fe/BC indicates that Co-Fe-functionalization changes the surface charges of BC Fig. 3(a), which facilitates electrostatic interaction with the anionic surfaces and may provide more active sites, enhancing biohydrogen production.

The electrochemical redox behaviour of PBC and metal-functionalized BC was characterized by CV, and the findings are shown in Fig. 3(b). Due to the distinctive shifts in the redox states of the catalyst's surface groups, the voltammograms appear to be featureless yet exhibit broad curvatures and potentials are referenced to RHE. A broad redox peak was observed in all BC electrodes, possibly owing to phenols and quinone groups on the BC surfaces. The lack of sharp peaks in the BC voltammograms implies the absence of the free metal particles on the BC surfaces, although the CV of the Co-Fe/BC reveals a redox peak centred near 0.34 V, and the redox current was 1.22 mA. Furthermore, the comparatively large integral area of the CV curve suggests that the Co-Fe/BC group has a greater specific capacitance (Gao et al. 2024). This may be expected because of the changes in the oxidation states of iron and cobalt species as Fe^{3+}/Fe^{2+} and Co^{2+}/Co^{3+} on the BC surface, as can be seen in the XPS analysis Fig. 2. The redox behavior of Co-Fe/BC was dominated by the redox species than PBC (0.59 mA), Co/BC (0.72 mA), and Fe/BC (0.99 mA). The height of the redox peak lowered in PBC, Co/BC, and Fe/BC, presumably due to either one-electron redox of the surface quinone-hydroquinone group or a reduction in surface functionality groups. A decreased electron transfer capability for PBC can be postulated because the functional groups on BC's surface are essential for the electron transfer process. Pyrogenic carbon derived from wooden biomass is characterized by surface functional groups, facilitating the accelerated direct intracellular electron transfer (DIET) mechanism associated with redox behaviour (Sathishkumar et al. 2020). In addition to providing adsorption sites for electron acceptors, BC transfers electrons and promotes the development of microorganisms, which directly correlates with improved catalytic activity.

LSV of PBC and metal-functionalized BC evaluating the electron transfer mechanism, the high current response showed that BC had good electrical conductivity, Fig. 3(c). For PBC, these electrodes have extremely low current densities, falling between 1.04 and − 4.16 mA/cm^2, the possible reason was that they had low SSA and no transition metal content. The current densities of Co/BC and Fe/BC electrodes were improved to 2.44 to − 3.84 mA/cm^2 and 1.37 to − 6.86 mA/cm^2, respectively. It is noted that compared with PBC, the current densities of Co/BC and Fe/BC electrodes were significantly increased, by increasing the SSA due to the loading of transition metals. Higher current densities ranging from 3.04 to − 6.89 mA/cm^2 were observed on Co-Fe/BC, verifying the promotion of Fe^{2+} for Co^{3+} reduction, creating OVs to maintain charge neutrality, thus enhancing EET (Guo et al. 2023a). The LSV current densities (Fig. 3c) indicate that the sharp drop in the low current density for all BC, particularly for Co-Fe/BC, is less pronounced than for other BC. A more considerable improvement in the BC current density was achieved by inserting iron and cobalt transition metals within the BC structure, as shown by the positive shift in the catalytic activity (Zhang et al. 2022). BC's high SSA and nano-porous size would help the PF by increasing the electrode–electrolyte contact area, allowing O_2 to diffuse and exposing more catalytically active sites. Meanwhile, pore size plays a crucial role; for instance, the micropore structure provides active sites that promote catalytic activity, while the mesopore structure supports microbial growth. Thus, an ideal combination of micropores and mesopores would enhance the electrochemical performance of BC.

The Nyquist plot can be utilized through the EIS analysis to ascertain the different BCs' resistance and gain insight into the kinetics of ion diffusion at the electrode–electrolyte interface, and all potentials are referenced to RHE. The EIS of the PBC, Co/BC, Fe/BC, and Co-Fe/BC were conducted at open circuit potential, from 10^5 to 1 Hz, and the results obtained are shown in Fig. 3(d). The Nyquist plot displays the imaginary part of impedance (-Z") against the real part (Z') over a range of frequencies (Xia et al. 2022). Each BC's charge-transfer resistance is directly proportional to the semicircle's diameter. Arc radius corresponds to the electron transfer efficiency, and it is widely recognized that the smallest radius decreases

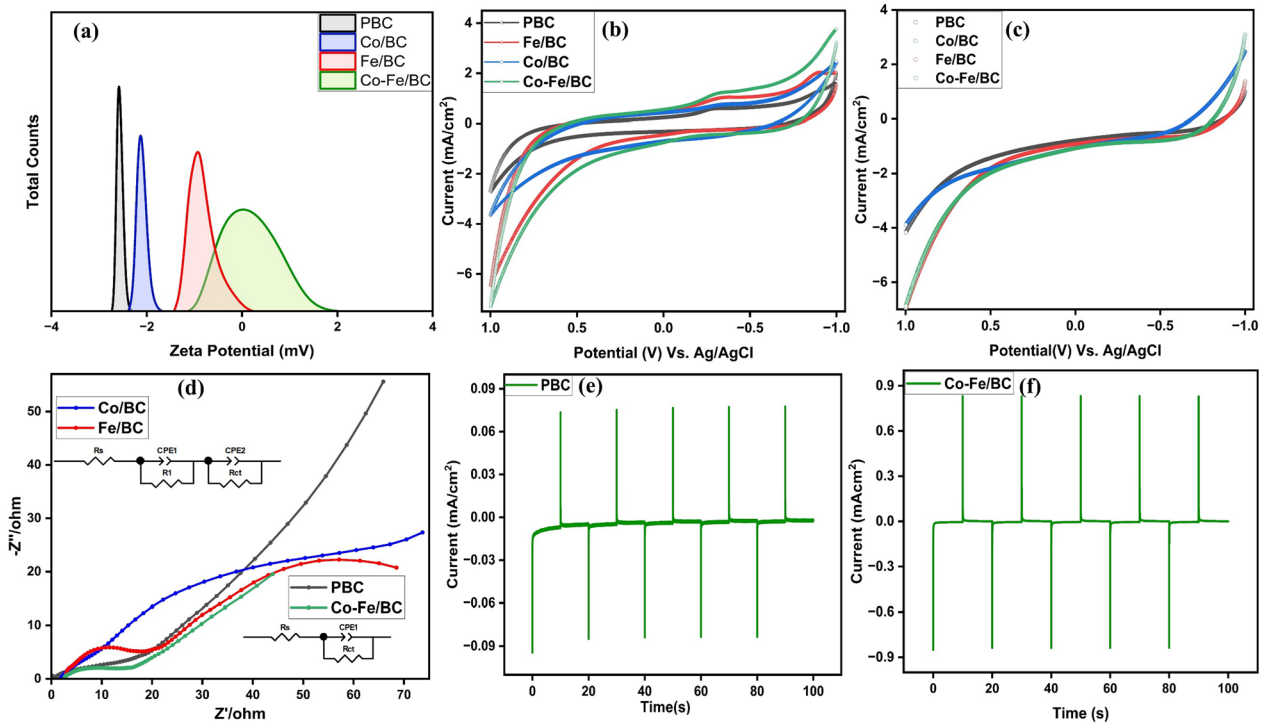

Fig. 3 Electrochemical characteristics of BCs. **a** Zeta potential measurements of PBC and metal functionalized BCs. **b** CV measurements. **c** LSV curves. **d** EIS spectra for PBC and metal functionalized BC. **e**, **f** Reductive and oxidative current responses of PBC and Co-Fe/BC

the transfer resistance and increases the electron transfer rate (Mei et al. 2018). The high photocatalytic performance of Co-Fe/BC was confirmed by its arc radius being smaller than that of PBC, which leads to a faster electron transfer (Eltaweil et al. 2022). The Randles' Model and modified double time constant equivalent model fitted the Nyquist plot in Zview software to calculate the parameters, including solution resistance (Rs), charge transfer resistance (Rct), constant phase element (CPE1, 2-T. CPE1, 2-P), the use of CPE accounts for the non-ideal, heterogeneous surface of the porous BC electrodes, and the modified circuit is given in the inset of Fig. 3d. The Rs values for PBC, Co/BC, Fe/BC, and Co-Fe/BC were recorded as 13.09Ω, 9.27Ω, 7.47Ω, 7.09Ω, respectively, which corresponds to the contact resistance of the current collector and the ohmic resistance of the interface. While the Rct values for PBC, Co/BC, Fe/BC, and Co-Fe/BC were recorded as 4.66Ω, 3.06Ω, 2.45Ω, and 1.74Ω, electron transfer was probably enhanced in Co-Fe/BC since it has the lowest Rct value as lower Rct values favoured electron transfer. The CPE1 (CPE1-T, CPE1-P) values for PBC, Co/BC, Fe/BC and Co-Fe/BC were recorded as ($1.69E^{-6}$ $F/s^{(P-1)}$, $4.12\ E^{-5}$ $F/s^{(P-1)}$, $3.89E^{-5}$ $F/s^{(P-1)}$, $2.77E^{-5}$ $F/s^{(P-1)}$) and (0.83, 0.75, 0.88 and 0.93) respectively. The CPE1-P value for Co-Fe/BC is close to 1, which indicates the ideal capacitor and the contribution of both the double layer and diffusion process, which indicates a favourable surface for facilitating electron movement via a conductive pathway and CPE1-T enhanced charge accumulation capacity (Atika And R.K. Dutta 2021). The CPE2 (CPE2-T, CPE2-P) values for Co/BC, and Fe/BC were recorded as ($1.47E^{-5}$ $F/s^{(P-1)}$, $6.62\ E^{-5}$ $F/s^{(P-1)}$) and (0.81, and 0.82) respectively. The knee frequency is illustrated as the utmost frequency at which the capacitive reaction is predominant, and resistance is negligible. Thus, the knee frequency of Co-Fe/BC (682 Hz) is higher than those of Fe/BC (563 Hz), Co/BC (464 Hz), and PBC (261 Hz), indicating that the first has a lower charge-transfer resistance compared to the second BC, this phenomenon is expected because PBC may not have many active sites while Fe/Co have catalytic sites that facilitate charge transfer (Xia et al. 2022; Wang et al. 2019). The EIS can be correlated with XPS, where the coexistence of Co^{+2}/Fe^{+3}, Co^{+3}/Fe^{+2}) oxidation states indicates a mixed valence system capable of facilitating electron transfer through redox transition (Abbas et al. 2023). The faster interfacial kinetics can be attributed to the synergistic effect of Co and Fe species. The EIS results having lower Rct for Co-Fe/BC are consistent with LSV results, which showed that Co-Fe/BC has more current densities.

BC possesses several redox groups and exhibits electron-transfer capability, potentially influencing its catalytic activity. The electron-accepting capacity (EAC) and electron-donating capacity (EDC) of PBC, Co/BC, Fe/BC, and Co-Fe/BC were examined using CA to analyze the impacts of electron transfer in BC. The redox current peaks of PBC and Co-Fe/BC illustrated that BC had both EAC and EDC Fig. 3e, f (Shu et al. 2022), EDC and EAC of Co/BC and Fe/BC can be seen in Fig. 2S(a, b). The electron-transfer capacity of Co-Fe/BC was demonstrated by its significantly higher EAC and EDC values than those of PBC, Co/BC, and Fe/BC. The Co-Fe/BC had a higher EDC of 8 mM e^-/g, than PBC (0.90 mM e^-/g), Co/BC (1.31 mM e^-/g), and Fe/BC (5.94 mM e^-/g), indicating that Co-Fe/BC more easily establishes a reductive environment which promotes the proliferation of more active sites. These findings suggest that Co-Fe/BC is more appropriate for promoting reactive species due to its enhanced electron-donating capacity; therefore, it is a potential candidate for improvement within the fermentative medium (Sathishkumar et al. 2020).

DPV explored extracellular electroactive mediators using CV as an alternative electrochemical approach with increased sensitivity/selectivity for studying electroactive shuttles. Redox-active compounds, including quinone, cytochrome C (c-Cyts), flavin, and rhibo/flavin, have been recognized as electron shuttles excreted by bacteria to promote biofilm EET and interspecies interactions. The DPV evaluation of PBC revealed distinct redox peaks at potentials of − 145 mV, − 280 mV, − 495 mV, and − 625 mV, which have been assigned to redox-active biomolecules, including cytochrome c-Cyts, c-Cyts/flavin interface, flavin, and riboflavin/FMN (flavin mononucleotide) complexes, respectively. These peaks reflect the interaction between EET dynamics and intracellular metabolic regulation, underscoring the role of redox mediators in bridging electron flux between extracellular environments and microbial respiration. In comparison, Co/BC and Fe/BC exhibited shifted redox peaks at − 115/− 105 mV, − 285/− 260 mV, − 470/− 425 mV, and − 645/− 605 mV, which suggest the emergence of tailored electroactive shuttles, likely mediated by the incorporation of transition metals, which modulate the redox behavior of electron carriers. The characteristic peaks at − 125 mV, − 235 mV, − 430 mV, and − 575 mV were detected in Co-Fe/BC, where c-type cytochromes facilitate electron transfer across membranes, with flavin acting as a free mediator in the EET process (Fig. 4). Their co-existence might suggest a pathway for electron transfer among electroactive bacteria during our fermentation process systems. Metal-specific interactions with extracellular biomolecules may improve electron transport efficiency or provide new redox pathways due to changed peak positions.

The point of concern was that compared with the PBC, the Co-Fe/BC oxidation peak current of c-cytochrome and Flavin increased from 4.754/5.129 μA to 8.708/9.599 μA with the positive shift of peak potential from − 145/− 495 mV to − 125/− 430 mV, respectively, indicating the promotion of metal based BC on the IET/EET pathway via c-cytochrome and flavin. It has been shown that IET/EET may occur directly between electroactive microorganisms via conductive carbon-based materials rather than depending on electrically conductive flavin/c-type cytochrome associated in biological interspecies electrical connections. Substituting conductive secretions with biochar might decrease the use of energy for electron transfer, which may be a major component in enhancing hydrogen generation (Jia et al. 2021). This shows how metal doping affects biochar electrochemistry and suggests engineering techniques to optimize electron exchange in bioelectrochemical interfaces.

3.4 Investigating the role of functionalized BC on PFHP

Figure 5(a, b) displays the effects of different concentrations of PBC and Co-Fe/BC, and Fig. 3S(a) of Co/BC and Fe/BC on H_2 production rate (HPR) and cumulative H_2 yield (CHY). It can be seen that the PFHP lasts for 12–48 h straight, and the CHY starts to stabilize after 48 h. This is because photosynthetic bacteria were barely inactive in the early stages of fermentation, and subsequently, the metabolism led to VFAs producing biohydrogen and saturation at the end of the experiment.

It was observed that bioreactors loaded with PCB concentrations of (0, 10, 20, 30, 40, and 50 mg/L), produced the HPR of (62.0, 65.67, 59.67, 52.74, and 47.85 mL/h), respectively. The highest HPR recorded was 65.67 mL/h at 36 h in the batch, with the bioreactor containing 20 mg/L of PBC, which is 15.76% greater than the HPR for CG, which stood at 62.00 mL/h. Functionalizing BC with Co and Fe enhances HPR, demonstrating maximum values of 71.77 and 79.16 mL/h when bioreactors are supplied with the optimal dose of 20 mg/L, respectively. Experimental results exhibited that the HPR increase at an optimal concentration (20 mg/L) with Co/BC was 16.97, which is 15.76% higher compared to CG and PCB. In contrast, the incorporation of Fe/BC produced 29.01, which is 27.68% higher HPR compared to CG and PBC, respectively, Fig. 3S(a). More importantly, when the BC was functionalized with dual metals (Co and Fe), there is a remarkable increase in HPR as the highest value of 123.69 mL/h was observed when the bioreactor was loaded with Co-Fe/BC concentration of 20 mg/L, whereas bioreactors loaded with concentration of 10, 30, 40, and 50 mg/L produced HPR of 72.0, 120.77, 112.51,

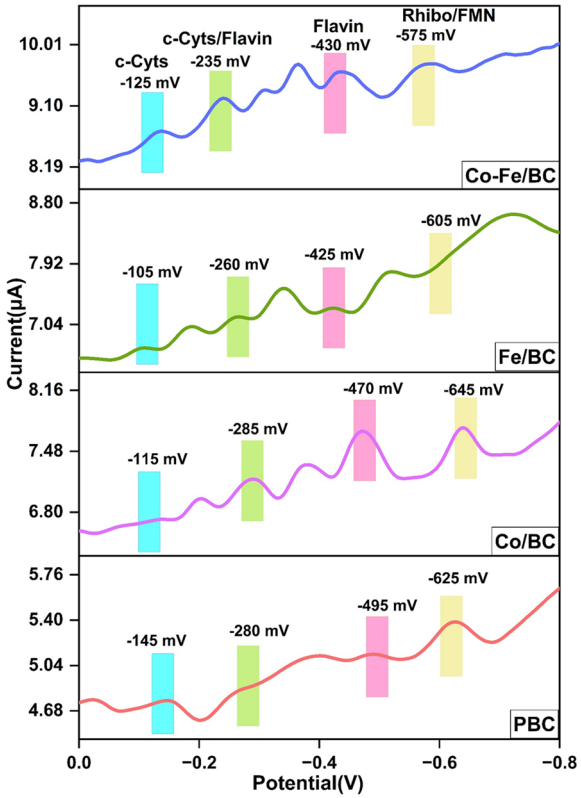

Fig. 4 Differential pulse voltammetry analysis to ascertain electron transfer in different BC system

and 85.57 mL/h respectively. Thus, CG has a maximum HPR of 61.36 whereas bioreactors loaded with optimal dose (20 mg/L) of Co-Fe/BC exhibited the maximum HPR of (123.69 mL/h), which was 101.61, 88.15, 72.34, and 39.11% higher compared to bioreactors of CG, PBC (65.74 mL/h at 30 mg/L), Co/BC (71.77 mL/h at), and Fe/BC (88.92 mL/h at) respectively, Fig. 5(c). The increase in HPR is related to the boost in photosynthetic bacteria's growth, accelerating the release from inactivity and increasing the production of biohydrogen. Adding BC can efficiently shorten the biohydrogen production period, as shown by the notably reduced lag time and the smaller duration of all BC's HPR curves compared to the CG (Ramzan et al. 2024). Although the incorporation of BC has a positive effect on biohydrogen production but an excess amount of BC could cause an inhibiting effect. The decrease in biohydrogen production with the incorporation of BC beyond their threshold concentrations can be related to an overdose of BC which potentially prevents light penetration (probably as a result of the accumulation and collision of BC grains) into the bacteria, eventually leading to retardation of cell growth (Meng et al. 2023). A threshold amount is generally required to optimize the quantity of BC required to positively impact pH, promote the proliferation of H_2-producing bacteria, and minimize the lag period of bacterial growth.

It is observed that the addition of functionalized BC also shows a remarkable effect on the CHY when bioreactors were incorporated with various concentrations of BCs, Fig. 5(b). Incorporating PBC with loading concentrations of (10, 20, 30, 40, and 50 mg/L) leads to CHY of (131.7, 131.86, 155.31, 142.14, and 143.25 mL) respectively. Whereas when bioreactors were loaded with functionalized BC of (Co/BC, and Fe/BC), the incorporation with doses (10, 20, 30, 40, and 50 mg/L) led to CHY production of (129.17, 176.43, 162.48, 124.86, 114.81 mL), and (125.2, 207.1, 199.21, 194.86, and 148.41 mL) respectively. It is worth noting that when BC was functionalized with dual metals of Co and Fe, the enhancement in biohydrogen production was remarkable as the incorporation of Co-Fe/BC with loading concentrations of (10, 20, 30, 40, and 50 mg/L) produced CHY of (149.50, 255.60, 217.72, 189.73, and 148.99 mL) respectively. Thus the highest CHY in bioreactors loaded with (Co/BC, Fe/BC, and Co-Fe/BC) at their optimal concentrations of 20 mg/L produced (176.43, 207.10, and 255.60 mL) which is (13.60%, 33.35%, and 64.57%) higher compared with PCB respectively. Whereas when compared with their respective CGs, the incorporation of optimal doses of (Co/BC, Fe/BC, and Co-Fe/BC) leads to an increase in CHY by (40.18, 64.55, and 103.10%), respectively, Fig. 5(d).

The remarkable increase in HPR, and CHY with functionalization of Co and Fe may be due to the fact of enhanced charge transfer capacity of the BC as dual metal functionalization increases the SSA, which leads to the formation of surface dangling bonds, hence the creation of OV which helps to transfer the charges more faster compared with the PBC. Creating OVs in Fe/BC is more endothermic than Co/BC due to the greater bond strength of Fe–O bonds than Co–O bonds, and the reduction of Fe^{3+} to Fe^{2+} releases less energy than the reduction of Co^{3+} to Co^{2+}. As a result of the introduction of holes (h+) in the Fe/BC, the OV concentration increases by several orders of magnitude. The low-spin state of Co^{3+} in Co/BC leads to the lowest OV formation energy among its near-degenerate magnetic configurations (Ritzmann 2016). Results depicted that the experimental groups showed remarkable performance in an order of Co-Fe/BC > Fe/BC > Co/BC > PBC > CG. The positive impact of the small amounts of cobalt and iron ions released from the surface of BC during the fermentation process can be attributed to the improved performance of dual metal functionalized BC. Therefore, a suitable concentration of co-functionalized BC can improve the HPR and reduce the PFHP's lag time, than other experimental groups, which is of great significance for PFHP.

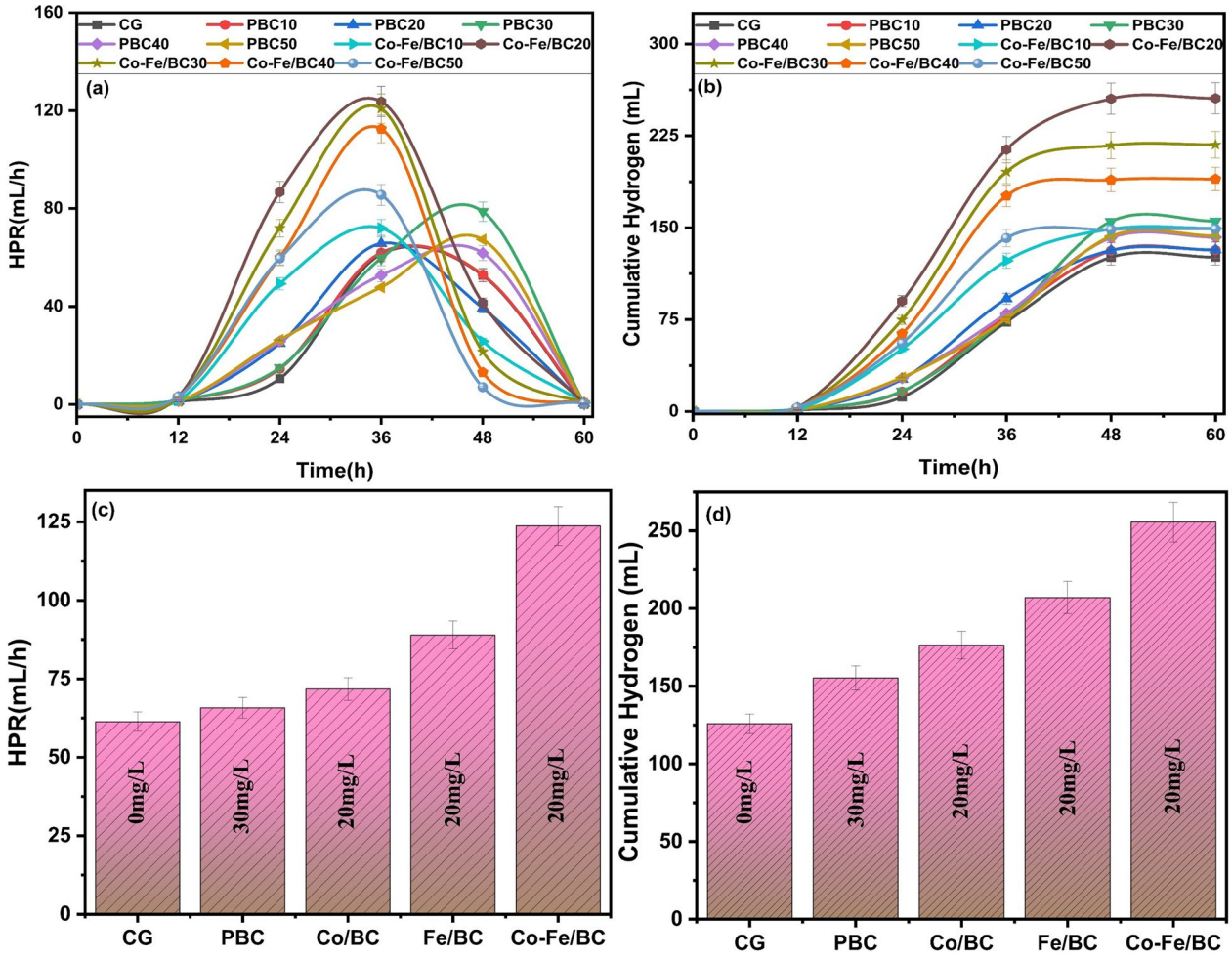

Fig. 5 Effect of BC on H_2 production characteristics: **a** H_2 production rate; **b** Cumulative H_2 yield; **c** HPR at optimal loading dose; **d** CHY at optimal loading dose

3.5 Effects of BC on the photo-fermentative pathway

Due to its buffering groups, such as phosphates, amino acids, and carbonates, BC can mitigate the accumulation of specific acids, improve the alkalinity of the fermentation media, and enhance the system's acid resistance. Changes in the soluble metabolites (SMs), such as ethanol and VFAs (mostly linked to acetate, butyrate, and propionic acid), usually accompany fluctuations in biohydrogen production across the whole fermentation process.

The addition of the various BC substantially enhanced the final SMs concentration in the fermentation process of the PBC, Co/BC, Fe/BC, and Co-Fe/BC groups, Fig. 6(a–e). The SMs fluctuation curves of PBC, Co/BC, Fe/BC, and Co-Fe/BC groups were almost similar, where the predominant SMs were acetate and butyrate, but their final SMs concentration varied. The CG produced 5.28 g/L SMs, which contained 2.77 g/L butyrate and 2.51 g/L acetate, following the butyrate pathway for hydrogen production (Liu et al. 2023b). The incorporation of Fe/BC and Co/BC produced 11.91 g/L and 10.91 g/L final SMs at an optimal loading concentration of 20 mg/L, respectively. The experimental results showed that observed SMs in bioreactors loaded with optimal PBC, Fe/BC, and Co/BC are 66.85%, 125.37%, and 106.62% higher than the CG, respectively. Whereas the final SMs in the bioreactor loaded with Co-Fe/BC group (20 mg/L) was 12.83 g/L with the dominant VFAs of acetate and butyrate, which is 154.58% and 41.15% higher than CG, respectively, where the propionic acid concentration in the Co-Fe/BC group was slightly lower than the CG. The findings presented that the (20 mg/L) optimum loading concentration of Co-Fe/BC significantly affects the metabolic rate, leading to 13.43%, 6.91%, 13.53%, and 16.63% higher SMs than other doses (10 mg/L, 30 mg/L, 40 mg/L, and 50 mg/L), respectively. The increase in SMs can be due to organic overloading at increased BC concentrations. The experimental results

are consistent with the previous finding (Sunyoto et al. 2016), which found butyric and acetic acid as the main VFAs at a lower BC loading of 8.30 g/L. At higher BC loading (> 12.50 g/L), propionate-producing microbes were activated in the mixed culture, which reduced the biohydrogen yield due to the consumption of biohydrogen in the propionate pathway.

The metabolic pathway shows that when ethanol and propionate were the metabolites, no biohydrogen was produced; hence, these metabolites somewhat decreased the biohydrogen yield. Because of the high acetate concentrations, the Co-Fe/BC group had the highest SMs concentration (2.68 g/L) at 24 h. Then SMs concentration declined to 2.35 g/L whereas the biohydrogen level increased, and remained steady in the final stages of fermentation, Fig. 6(e). This could be due to BC's greater SSA absorbing part of the fermentative broth's metabolites to prevent acidification and enable bacterial metabolism, preserving the system's stability (Guo et al. 2023b). Due to lower SSA than Co-Fe/BC, the PBC group continued to have less acid gathering throughout the fermentation process, particularly for acetate and butyrate, and their ultimate total concentration was just 8.81 g/L, which was 31.33% lower than Co-Fe/BC. Experimental findings suggested that supplementing Fe and Co by efficiently using acetate and butyrate may regulate the pH, leading to an increase in the biohydrogen yield. Previous research findings revealed that BC derived from rice straw enhanced glucose degradation and biohydrogen productivity because conductive NDBC reduced the EtOH pathway, whereas the HAc and HBu pathways were selectively enhanced, consistent with our results (Li et al. 2020b).

Appropriate concentrations of SMs might provide moderate pH conditions because it is known that some functional groups on the BC surface functioned as pH buffer during biohydrogen generation (4.5–6), facilitating microbial growth and producing high biohydrogen yield by converting BA to AA pathway Fig. 6(e) facilitated by DIET. Biohydrogen is rapidly produced following the acetate and butyrate pathways, but high-carbon metabolite accumulation could lead to a significant drop in pH, which harms the microorganisms. As a result, acetate-type development becomes more prevalent, reducing excess H^+ and increasing stable biohydrogen production. Thus, butyric acid is generally directly linked with the biohydrogen generation rate, whereas acetic acid positively correlates with the accumulated biohydrogen yield. Biochar's inherent pH buffering ability, in line with Li et al.'s findings, is vital for reducing typical acid inhibition and maintaining an optimal pH environment that selectively encourages the growth and enzymatic activity of microorganisms in the acetic acid pathway, thus lowering butyrate production (Li et al. 2025). Therefore, in our photo-fermentative system, the combined effect of biochar's pH buffering and its advanced EET capabilities drives a key metabolic shift from the less efficient butyric acid pathway to the more hydrogen-yielding acetic acid pathway. Similarly, for the *C. tyrobutyricum* in the anaerobic digestion system, acetate (53.31%) and butyrate (26.60%) were produced by BC addition, which resulted in 44.81% enhancement in HY (Li et al. 2020b). The facts showed that BC either influenced bacterial abundance and community structure or facilitated the transfer of electrons during biohydrogen development. Another explanation for DIET is that the butyrate-oxidizing bacteria utilize BC as the transient electron (e^-) acceptor in the dormant metabolism of methanogenic archaea to oxidize butyrate to acetate.

3.6 Effect of BC on ORP, RS, and pH

The ability of anaerobic fermentation is linked to the oxidation–reduction characteristics of fermentation broth, and the redox potential may show how free electrons in the broth react when used as a medium in the PFHP process. It has been seen that all the bioreactors loaded with BCs showed more negative ORP values between 0-36 h as compared to the bioreactor of CG, which is possibly correlated to the photogenerated e^- generated by Co and Fe functionalized BC involved in PFHP, Fig. 4S(a, b) (Nadeem et al. 2020). It was observed that the PBC obtained (−416 mV) ORP, and the lowest ORP (−502 mV) at 24 h was obtained for the Co-Fe/BC at 20 mg/L optimal loading concentration, which was 23.07, and 65.69% lower compared to the CG (−309 mV), respectively. It can also be seen that co-functionalized BC obtained 10.10%, and 8.41% lower ORP than Fe/BC and Co/BC, respectively, Fig. 4S (a, b). The findings show that the co-functionalized BC can improve PFHP by enhancing the reducing environment, strengthening the capacity of H^+ for capturing e^-, and increasing biohydrogen production. This phenomenon results from the previously described changes, in which the Co and Fe introduced additional redox-active sites, leading to an enhancement in the catalytic activity of the BC also high SSA and the well-developed porous structure can facilitate active sites for photocatalytic reactions, facilitate ion diffusion, and enhance the PFHP performance (Nadeem et al. 2020).

The variation in RS concentration during the fermentation process can also affect the PFHP efficiency. As can be seen from Fig. 4S(c), the CG obtained the RS (2.26 g/L) at 12 h after that the RS started to decrease, while the experimental group with Co-Fe/BC obtained the highest RS (6.45 g/L) at 12 h. It is observed that in comparison to Fe/BC, Co/BC, PBC, and CG, the incorporation of Co-Fe/BC enhanced the sugar by 25.97%, 51.40%,

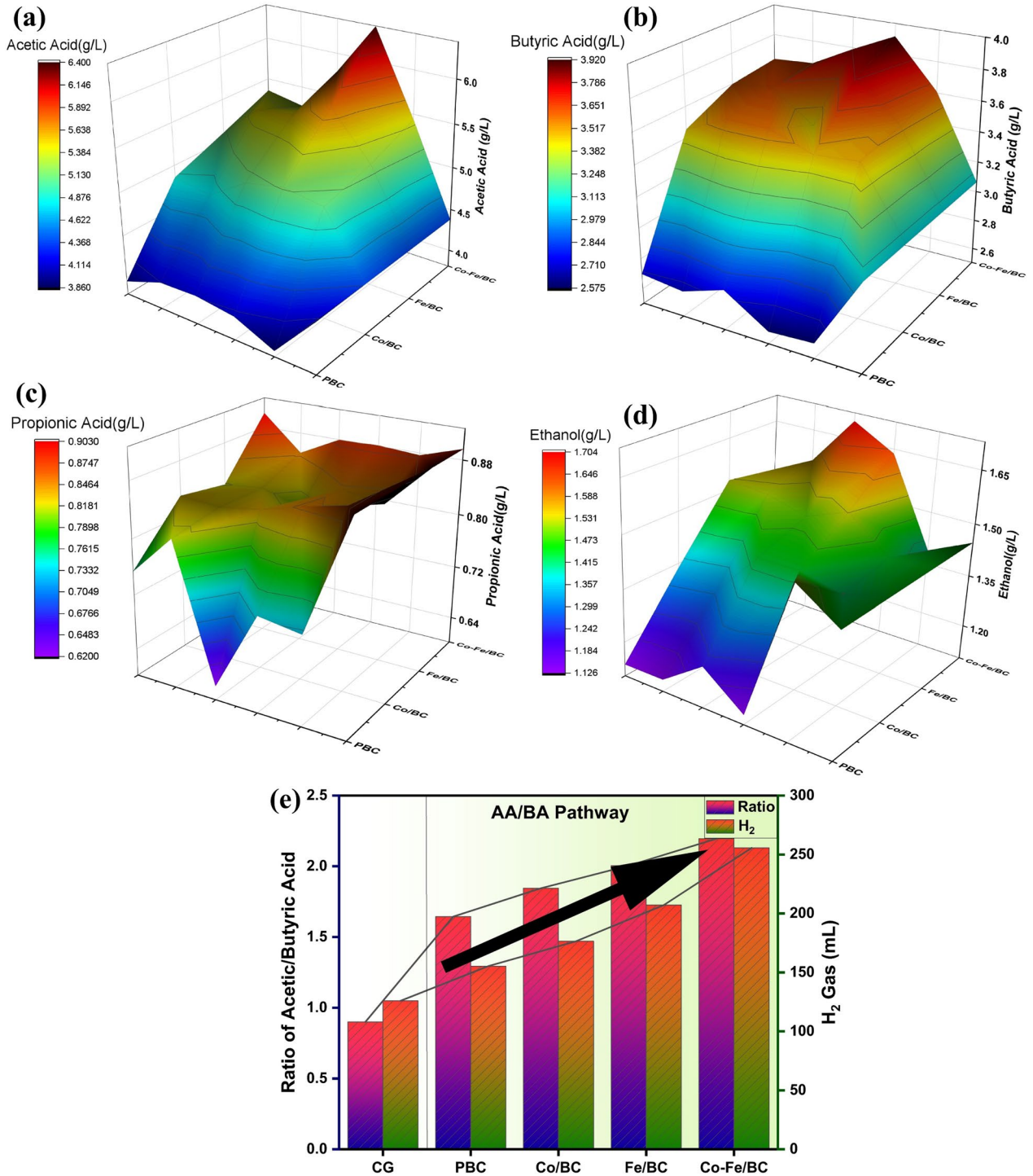

Fig. 6 Effect of BC on soluble metabolites resulting from PFHP: **a** Acetic Acid, **b** Butyric Acid, **c** Propionic Acid, **d** Ethanol, and **e** Acetic/Butyric Acid ratio of CG and BCs

85.34%, and 185.39%, respectively, which is 2.85-fold higher compared to CG. Moreover, the incorporation of Fe/BC, Co/BC, and PBC reduced the sugar by 2.26, 1.88, and 1.53-fold compared to the CG, respectively. This may be because the incorporation of BC improved PNSB's usage of light energy and reduced the inactivity time. PNSB was able to use the RS following cellulose digestion quickly and convert them into VFAs for the biohydrogen

production, whereas the CG had a more extended delay period. It was noticed that during the entire fermentation process, bioreactors loaded with Co and Fe co-functionalized BC reduced higher sugars compared with other experimental groups. This may be due to the high activity of PNSB at Co and Fe functionalized BC, which has a strong ability to metabolize RS to acids and can provide indispensable nutrients for microbial growth by improving the activities of hydrogenase and biohydrogen production (Usman et al. 2024).

The effect of BC on PFHP and RS consumption may be attributed to the fact that incomplete RS consumption occurs when pH levels decline significantly as a result of acid accumulation. As shown in Fig. 4S(d), after 24 h the pH values of each group was in the acidic range (4.99–5.80), due to the rapid conversion of RS into VFAs, when the PNSB was inactive and had not yet used the VFAs to produce biohydrogen at the start of fermentation, leading to the acid accumulation. After 24 h, the BC-containing groups stabilized the system pH due to their buffering capacity, produced biohydrogen by consuming the VFAs, and converted RS to produce acids, which were in a dynamic equilibrium. It is observed that during the initial time (24 h), the pH of the Co and Fe co-functionalized BC was the lowest as compared to other experimental groups (CG, PBC, Co/BC, and Fe/BC) which produced pH of 5.70, 5.41, 5.14, and 5.12, respectively. This variation in pH suggested that excessive amounts of Co and Fe functionalization on BC might hinder light penetration into the bacterium and cause cell development retardation, most likely as a result of BC grains colliding and accumulating. Thus, a suitable co-functionalization of both metals may positively affect pH, H_2-producing bacterial growth, biofilm formation, and lag phase shortening (Li et al. 2020b).

3.7 Kinetic model of functionalized BC for biohydrogen production

For better understanding and investigation, the kinetic parameters P, R_{max}, and x were studied to evaluate the performance of CG, PBC, Co/BC, Fe/BC, and Co-Fe/BC in PFHP. The (P, R_{max}, and x) kinetic parameters obtained are summarized in Table 2 by fitting the modified Gompertz model. The R^2 values above 0.99 indicate a good agreement between theoretical predictions and experimental results, Fig. 5S. Using the optimal concentration of Co-Fe/BC (20 mg/L), the time it takes to produce biohydrogen is significantly shorter than that of the CG.

The bacterial growth rate increases as the nutrient concentration increases until it reaches an inhibitory level, at which point the growth rate drops. The saturation constant, K_s, shows the impact of the CG and BC groups on bacterial growth from the Monod equation. The saturation constant, K_s, indicates the concentration that sustains half-maximal bacterial growth under certain conditions. This model suggests that the PFHP process employs sugar metabolism, consistent with the high sugar usage shown in Fig. 4S(c). The optimal growth rate occurs when the substrate concentration (S) in the Co-Fe/BC exceeds the $K_{s,}$ and all required nutrient concentrations are equal in all experimental groups.

3.8 Effects of the functionalized BC on the bacterial community structures

The relationship between the supplementation of various functionalized BC and the community structure of microbes is a critical indicator of biohydrogen production. To further study the influence of functionalized BC including CG, PBC, Co/BC, Fe/BC, and Co-Fe/BC, we conducted a phylogenetic analysis of (16S rRNA) gene sequences to determine the composition of the microbial community and the results are shown in Fig. 7 and Fig. 6S (a, b). It was observed that the bacteria were sensitive to BC supplementation and functionalized metals, resulting in a greater diversity of the bacterial community compared to the CG. The increase in diversity was evident at both the phylum and genus levels in the samples of CG, PBC, Co/BC, Fe/BC, and Co-Fe/BC. According to the phylogenetic categorization at the phylum level, Firmicutes, *Bacteroidetes, and Chloroflexi dominated* the three samples; however, the abundance of each sample differed (Fig. 7(a). In CG trials, Firmicutes (88.25%), Proteobacteria (4.72%), and Bacteroidetes (7.19%) were found in major part, while Synergistetes (0.24%), Actinobacteria (0.7%), Patescibacteria (0.04%), Chloroflexi (0.009%), and others (0.003%) were found in minor and main bacterial phyla of the total bacterial sequences Fig. 7(a).

The majority of studies have supported the assertion that Firmicutes bacteria have a superior capacity to ferment and metabolize carbohydrates and lipids. Researchers have attributed this to the fact that certain bacteria of the Firmicutes phylum, which produce a greater number of enzymes responsible for carbohydrate degradation and fermentation (Stojanov et al. 2020). Firmicutes seemed to be the most prevalent phylum among all groups, with a proportion of 84.27%, 82.83%, 81.19%, and 79.42% in the CG, PBC, Co/BC, and Fe/BC and Co-Fe/BC, respectively. The fermentation condition was primarily enhanced by the buffering capacity of the biological systems under the addition of BC, as indicated by the reduced level of Firmicutes in bioreactors; other phyla flourished under supplementation and enhanced the depolymerization of biomass to produce the monomers, which facilitated enhancement in biohydrogen production. While some strains cannot recover from the thermal shock process,

Table 2 Kinetic analysis of functionalized BC for biohydrogen production

Model	Modified gompertz model				
Plot	**CG**	**PBC30**	**Co/BC20**	**Fe/BC20**	**Co-Fe/BC20**
P (mL)	133.37449 ± 6.19846	169.28334 ± 14.57005	183.32619 ± 5.08632	219.54452 ± 9.63345	260.16631 ± 3.04997
R (mL/h)	17.55771 ± 2.54286	20.06819 ± 4.72023	20.55668 ± 1.99558	24.90059 ± 3.01323	37.10338 ± 2.09132
X (h)	23.95048 ± 1.59393	24.58962 ± 2.7071	20.82218 ± 1.13643	19.76729 ± 1.36507	17.40402 ± 0.50689
R^2 (COD)	0.99524	0.99784	0.99821	0.99616	0.99957
Adj. R^2	0.99207	0.99639	0.99701	0.99359	0.99928
Model plot			Monod model		
R^2	0.97818	0.99883	0.99391	0.99921	0.99968

Firmicutes can produce endospores to adapt and resist a harsh microenvironment. Firmicutes can produce biohydrogen by utilizing glucose, and they contain a variety of H_2-producing bacteria (HPB) (Liu, et al. 2023). Under specific conditions, Firmicutes can redirect their metabolic emphasis from butyrate synthesis to alternative short-chain fatty acids such as acetate. This may arise from alterations in substrate availability or environmental circumstances. For example, in the presence of more easily fermentable carbohydrates, the metabolic pathways may preferentially produce acetate instead of butyrate (Houtman et al. 2022). Firmicutes' primary function was to ensure the system's stability. The addition of BC improved the system's buffering capacity, while the addition of functionalized BC stabilized and enhanced the diversity of the microbial community.

Bacteroidetes and Proteobacteria were the next most abundant phyla after the Firmicutes in all BC-supplemented systems, including CG (4.72%, 7.19%), PBC (5.84%, 9.68%), Co/BC (5.24%, 11.52%), Fe/BC (5.33%, 13.13%), and Co-Fe/BC (4.44%, 14.0%), respectively. Simple polysaccharides and monosaccharides might be fermented into VFAs by the physiologically varied species of the improved Proteobacteria phylum. Within the Bacteroidetes phylum, Bacteroides is an anaerobe essential for converting organic substances into acetate, biohydrogen, and CO_2. According to previous research, Bacteroidetes and Firmicutes both have significant but distinct functions in biomass breakdown. Firmicutes are more likely to play a pivotal role in the initial cellulose cleavage stage, while Bacteroidetes play a larger role in the subsequent hemicellulose decomposition. The generation of the SMs caused a drop in pH early in the experiment, and HPB's consumption of the SMs for growth and biohydrogen production was associated with a later rise in pH. Under the supplementation of PBC, Co/BC, and Fe/BC, the abundance of these phyla altered and caused minor enhancement (Fig. 6S), but the functionalization of Co-Fe/BC had a more profound effect on their community: Synergistetes (0.99%), Actinobacteria (0.23%), Patescibacteria (0.52%), and Chloroflexi (0.293%).

Relative abundance analysis at the genus level demonstrated a significant shift in microbial community composition during the fermentation. Dominant genera included *Clostridium_sensu_stricto_1, Clostridium_sensu_stricto_11, Proteiniphilum, Clostridium_sensu_stricto_12, Enterococcus, Rummeliibacillus, Rhodopseudomonas, Clostridium_sensu_stricto_13, Tissierella, Sporanaerobacter, Paraclostridium, Lentimicrobium,* and *Bacillus* Fig. 7(b). Biohydrogen producing genus *Clostridium* was the most abundant genus (79% to 89%) in all bioreactors CG (79.77%), PBC (83.62%), Co/BC (86.54%), Fe/BC (84.63%), and Co-Fe/BC (83.24%). *Clostridium* is a common genus that specializes in fermentative biohydrogen production and can generate biohydrogen from glucose, sucrose, and xylose (Liu, et al. 2023). The relative abundances of *Clostridium_sensu_stricto_1, Clostridium_sensu_stricto_12, Clostridium_sensu_stricto_13*, and *Clostridium_sensu_stricto_11* in the CG were 76.06%, 2.75%, 0.85%, and 0.09% in CG, respectively. The highest *Clostridium* genus abundance was found in PBC, Co/BC, Fe/BC, and Co-Fe/BC, at 79.77%, 80.52%, 86.03%, and 86.72%, respectively. *Clostridium_sensu_stricto_1* (75.13%, 78.51%, 77.50%, 70.01%), *Clostridium_sensu_stricto_12* (7.51%, 8.06%, 9.06%, 11.06%), *Clostridium_sensu_stricto_13* (0.88%, 1.92%, 1.92%, 2.02%), and *Clostridium_sensu_stricto_11* (0.09%, 0.10%, 0.12%, 0.142%) was found in PBC, Co/BC, Fe/BC, and Co-Fe/BC, respectively. The genus *Clostridium* is well-documented and recognized for its capacity to generate biohydrogen form lignocellulosic biomass. (Wang And Yin 2021).

Rummeliibacillus, Tissierella, Sporanaerobacter, Paraclostridium, and *Bacillus* genera were found (0.7– 1%,

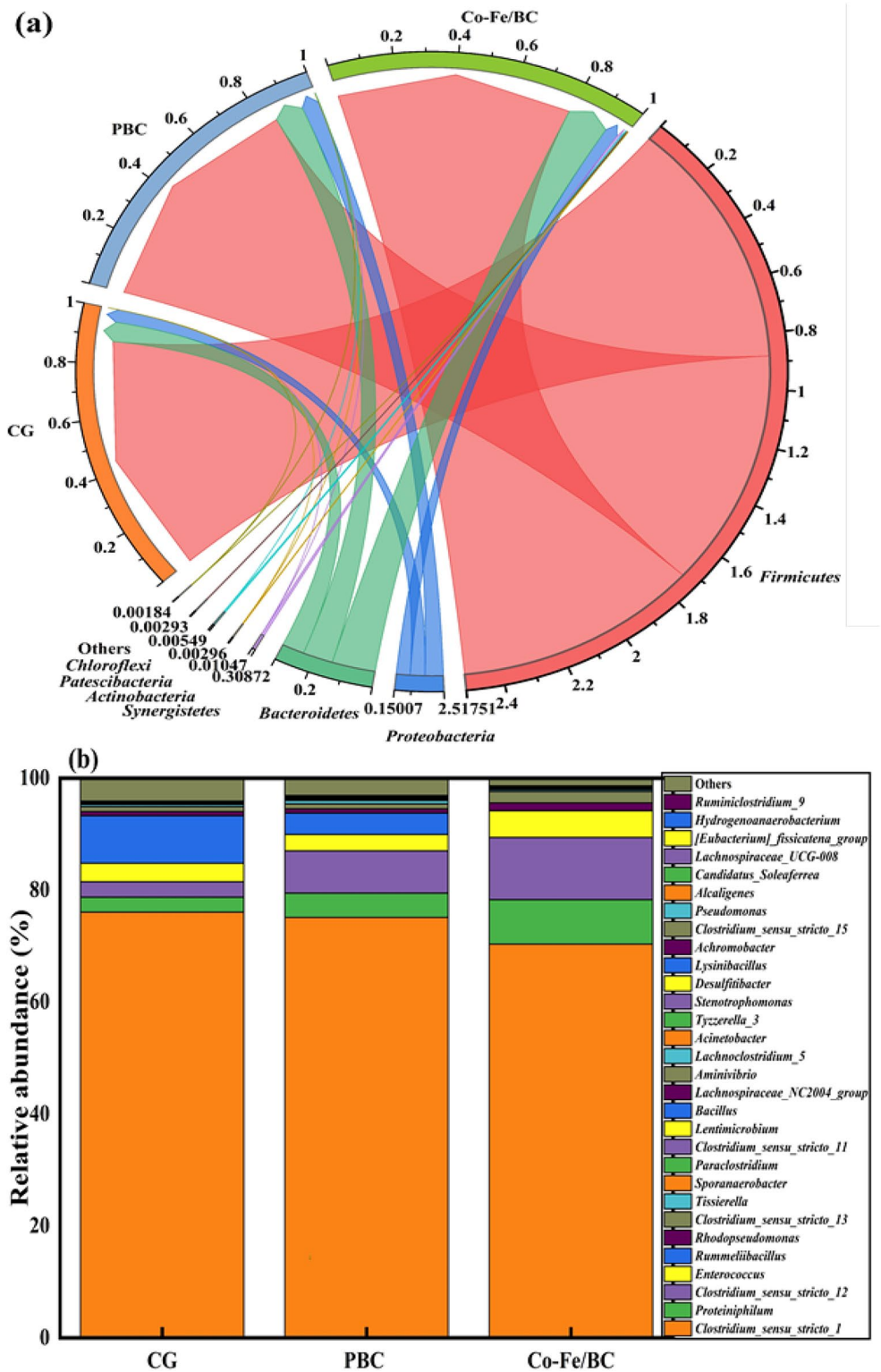

Fig. 7 Effect of BCs on microbial community: **a** phylum level, **b** genus level

0.2–0.7%, 0.09–0.22%, 0.02–0.2%, 0.01–0.11%, 0.05–0.06%) in all groups; these genera were responsive to the addition of BC. After *Clostridium,* the dominant genera were *Proteiniphilum* and *Enterococcus,* with abundances of (2.67%, 3.32%), (4.34%, 2.95%), (6.21%, 1.85%), (4.12%, 3.95%) and (7.9%, 4.73%) in CG, PBC, Co/BC, Fe/BC, and Co-Fe/BC, respectively. *Proteiniphilum,* the sole significant bacterial genus in the Bacteroidetes phylum, also eventually exhibited the oxidation pathway of acetate. At present, it is regarded that the role of *Proteiniphilum* species is limited to hydrolysis and fermentation (Feng et al. 2023). The *Enterococcus* genus, part of the phylum Firmicutes, represents a complex and evolving group of microorganisms. *Enterococcu*s has been identified as a genus that produces a small amount of biohydrogen gas, according to certain research. However, other studies have revealed that acetate is the primary fermentative metabolite produced by *Enterococcus*, a group of lactic acid bacteria that may generate lactate, ethanol, and acetate as the end products of carbohydrate metabolism (Canto-Robertos et al. 2023). The previously described three genera were also identified in different anaerobic fermenters where loading with BC enhances the biohydrogen production through changing metabolic pathways from butyrate – H_2-type fermentation to acetate – H_2-type fermentation. Thus, the addition of BC enhances the hydrogen-producing bacterial community, whereas engineering its microbial-electrochemical interface through (Co and Fe in the present case) enhances microbial diversity, which fosters a mutualistic relationship between the consortium and enhances diversity and EET, leading to enhanced biohydrogen production.

Based on the experimental results (Fig. 1, Fig. 3, and Fig. 4), the effect of engineering surface of the PBC through Co and Fe can be conceptualized through Fig. 8, where the presence of Co and Fe at the interface provides electron-conducting channels in functionalized biochar, helping to increase the EET and metabolic rate, eventually leading to increased biohydrogen production. The use of 900 °C was critical to achieving a highly conductive carbon graphitized carbon matrix and stable Co-Fe nanostructure. Lower temperatures result in BC with poor conductivity, unstable metal dispersion, and insufficient OVs, factors that limit microbial-electrode interaction and catalytic performance. Co was chosen due to its redox activity (Co^{2+}/Co^{3+}), its ability to facilitate rapid electron transfer, and its catalytic role in the biohydrogen production mechanism. Co also interacts favorably with outer-membrane redox proteins, such as cytochromes and flavins, thereby enhancing EET (Jiang et al. 2023). Biohydrogen generation is an oxidation–reduction process where H^+ accepts electrons and is reduced to produce biohydrogen. EET transfers electrons to H^+, and this transfer efficiency significantly influences the yield and rate of biohydrogen generation. According to earlier research, EET has a greater electron transfer rate (44.9×10^3 e^- /cell pair/s), and is thought to be a more stable and efficient channel, and conductive materials have been used to enhance it (Gu et al. 2023). The combination of Co and Fe creates a synergistic redox environment, as signified by XPS, where Co and Fe contribute to mutual valence cycling and increased OVs formation. The EET energy demand is achieved by Co-Fe functionalization on BC, and microbial syntrophic interactions, Fig. 7. The remarkable increase in biohydrogen production is due to an enhancement in the charge transfer capacity of the Co-Fe/BC, which not only offers a significant SSA and a very porous structure that sustains cellular viability. Co-Fe/BC proved vital to EET because its Fe and Co function as electron conductors in a photo-fermentative system, providing a direct electron transfer pathway and encouraging DIET, which raises the EET by drastically lowering the energy requirements of microorganisms, boosting metabolic activity, and improving biohydrogen yield. The results were further supported by the CV measurements which show that surface functionalization with dual metals of Fe and Co has higher current density as compared to the Co/BC, Fe/BC, and PBC, which could be due to the large SSA and the presence of additional charge carriers such as OVs which favors the biohydrogen production (Nadeem et al. 2020). Dual metal functionalization can replace the catalytically active metal ion center, forming OVs by charge compensation. The formation of OVs on the BC surface leads to the generation of one or two electrons that interact with the substrate molecules. The electrochemical results showed that BC with redox active sites showed superior electrical conductivity and reduced charge transfer resistance, thus enhancing the catalytic performance. Moreover, mesoporous structures stimulate microbial growth while micropore structures provide active sites for enzymatic activity; thus, BC electrochemical performance would improve with the combination of micropore-mesoporous structures. Furthermore, it was observed that Co-Fe/BC conceptualized as EEMs, facilitating enhanced electron flux across microbial species and thereby accelerating microbial metabolic pathways favorable for catalytic activity and hydrogen production (Yu et al. 2025).

In addition, Fe^{3+} regulates the community of microbes and improves hydrogenase activity, and the fermentative bacteria could grow freely on the BC's surface and inside its porous structure, forming a biofilm. Fe^{3+} and Co^{2+} free radicals attack glycosidic linkages in biomass, leading to dehydration, decarboxylation, and condensation processes during high-temperature (900 ℃) pyrolysis; this

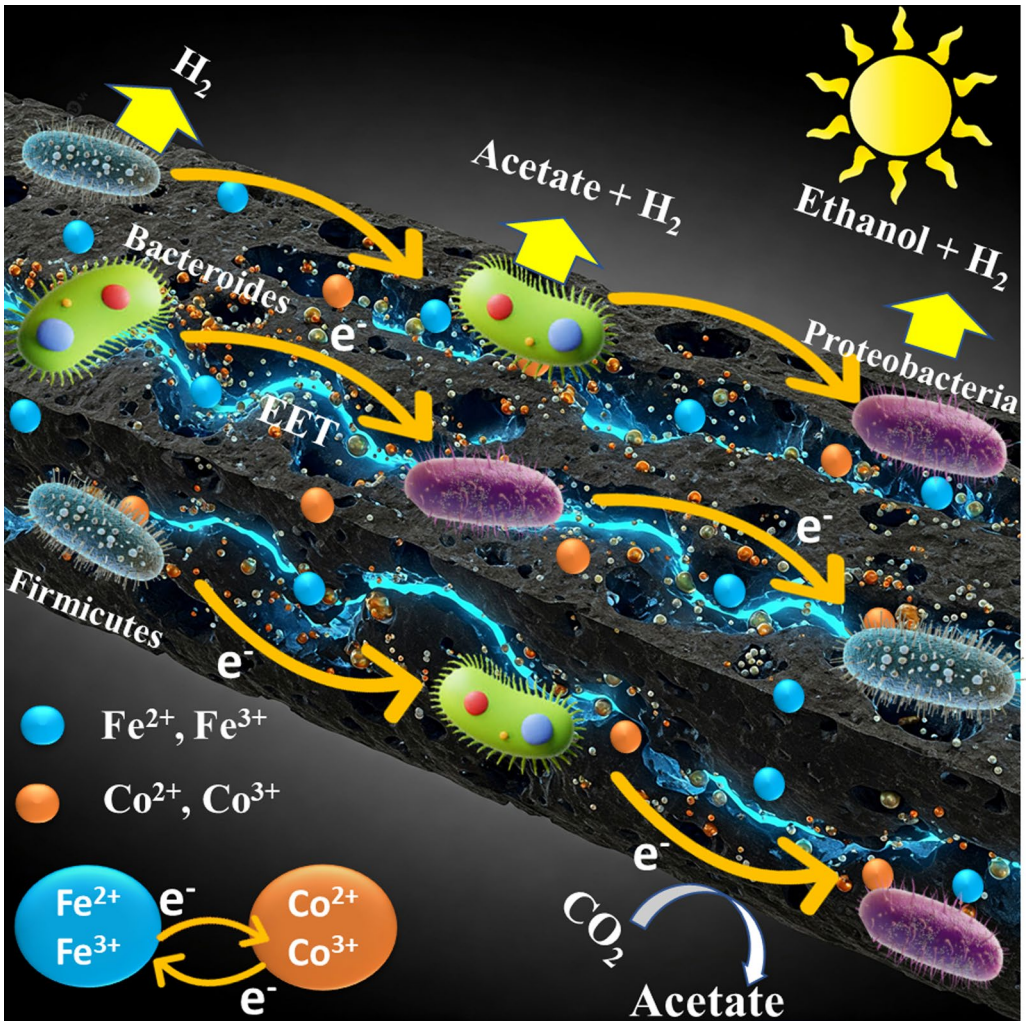

Fig. 8 The proposed mechanism of BC working as an extracellular electron transfer for biohydrogen production

enhances the defects and oxygen-containing functional groups of BC. The above method also produces reducing gases, facilitating the reduction of Fe^{3+} and Co^{2+}. The iron oxide reduction may consume adjacent carbons at elevated temperatures, resulting in lattice expansion and increasing the pore volume of BC, and resulting in a multi-stage porous structure with enhanced SSA. Thus, the homogenous dispersion of Co-Fe/BC in the fermentative medium provides more contact area of engineered BC to the microbes and facilitates the attachment of microbes, leading to an increase in their growth (Di et al. 2022). In addition, the interconversion between Fe^{2+}/Fe^{3+} could improve the activity of [Ni–Fe] and [Fe–Fe] hydrogenases, and in ferredoxin, where ferritin serves as both a proton reductant for H_2 molecules and an electron carrier for pyruvate oxidation to acetyl-CoA and CO_2, the presence of Co^{2+} inhibits the accumulation of SMs, thereby effectively enhancing the biohydrogen yield (Mikheeva et al. 2022). The pyruvate ferredoxin oxidoreductase (PFOR) enzyme enhances the conversion process of pyruvate into acetyl-CoA under anoxic conditions; at the same time, it reduces ferredoxin from Fd to FdH (FdOx-FdRed) (Ji And Shen 2024). This FdH carries the electrons released when the substrate is oxidized to the hydrogenase so that the hydrogenase can reduce the proton to biohydrogen. When glucose is converted to pyruvate, the generated NADH serves as the precursor in an alternative path (the NADH pathway), and is oxidized by PFOR and NADH-dependent hydrogenases to produce H_2. Compared to the NADH system, the formate pathway is more sensitivity to pH variations. At pH 7–7.5, the formate pathway produced the maximum H_2, but at lower pH levels below 5, it produced less. However, there was no apparent decrease in biohydrogen generation by the NADH route in response to the system pH shift (5–7.5), Fig. 4S.

Furthermore, the increase in biohydrogen production by incorporating engineered BC can also be supported by the experimental findings of metabolic by-products, where it was observed that the incorporation of engineered BC altered the metabolic pathway from the BA to the AA pathway, Fig. 6(e). The biohydrogen production shifts its metabolic pathway from butyric acid to acetic acid as described by theoretical Eqs. (4) and (5) (Noguer et al. 2022).

$$C_6H_{12}O_6 + 2H_2O \rightarrow 2CH_3COOH + 2CO_2 + 4H_2 \Delta G = -206\ \text{kJ} \quad (4)$$

$$C_6H_{12}O_6 \rightarrow CH_3CH_2CH_2COOH + 2CO_2 + 2H_2 \Delta G = -254\ \text{kJ} \quad (5)$$

Simultaneously, the Co and Fe released by Co-Fe/BC may optimize the expression of PF functional genes and improve both the electron transfer and the glucose conversion rates. The experimental findings of microbial community analysis confirmed that Firmicutes were the primary biohydrogen producers in the PF system, and the incorporation of Co-Fe/BC might enhance the abundance of Firmicutes within the microbial community. The metabolic shift in Clostridium results from a behavioural alteration within the same microbial population, driven by pH-dependent adaptation mechanisms in the Clostridium genus that lead to the preferential production of acetic acid and butyric acid. The optimum pH is different for each species or enzyme, which leads to varied bioreactions with changes in pH. In addition, the Gibbs free energy of reaction is influenced by the pH values, which suggests a significant effect of pH on responses from the thermodynamic perspective. It is generally concluded that acetic-butyric type fermentation always occurs at a pH range of 5.7–7, and acetic-propionic type fermentation dominates at pH values ranging from 5.0 to 6.0. In comparison, a low pH range < 4.5 favours acetic-ethanol-type fermentation (Jiao et al. 2022).

Thus, engineering of the microbial-electrochemical interface between host biochar and its composites with dual metals represents a promising roadmap for enhancing the biochemical conversion of lignocellulosic biomass. The exceptional physicochemical properties, along with the synergistic interaction between carbon and metal nanomaterials at the interface, enable them to facilitate electron flow in various crucial stages of the biochemical conversion of the biomass. Therefore, selecting appropriate material for functionalization is of utmost requirement for the formation of continuous conducting channels, which enhances the charge transfer within the fermentative medium during PFHP by regulating the metabolic pathway.

4 Conclusion

The microbial-electrochemical interface of the biochar was altered through dual metal (Co and Fe) surface functionalization to enhance the charge transfer capacity. Experimental findings showed that in comparison to single metal functionalization (Co/BC, Fe/BC), functionalization with Co-Fe/BC enhances the porosity and SSA, which provides more active sites and surface defects such as OVs for enhanced charge transfer. Optical and electrochemical characteristics suggested that due to the presence of redox-active groups, Co-Fe/BC possesses a lower interfacial charge transfer resistance leading to higher redox current compared with PBC, Co/BC, and Fe/BC, thus increasing the EET. Due to enhanced charge transfer capacity, Co-Fe/BC increased biohydrogen production by 103.1%, 64.59%, 44.88%, and 23.34% compared to the CG, PBC, Co/BC, and Fe/BC, respectively. The remarkable increase in biohydrogen production is related to the regulation of metabolism during the fermentation process, as Co-Fe/BC alters the metabolic pathway from butyric acid to acetic acid. Moreover, large SSA and surface functionalization with Co and Fe provide a growth medium for the bacterial community, as the microbial community analysis demonstrated that *Clostridium* was the most abundant genus at 86.72%. Co-Fe/BC makes microbes attach to it firmly and promotes cell growth faster, whereas Fe^{3+} facilitates hydrogenase activity, and Co^{2+} is capable of electron transfer and rearrangement. Thus, altering the interface between microbes and biochar can be an effective pathway to enhance the charge transfer within the fermentative medium, which eventually boosts the electron transfer rate responsible for increasing metabolic rate and biohydrogen production.

Supplementary Information

The online version contains supplementary material available at https://doi.org/10.1007/s42773-025-00539-y.

Supplementary material 1

Author contributions

Nadeem Tahir: conceptualization, supervision, funding acquisition, review, and editing. Hina Ramzan: methodology, formal analysis, investigation, visualization, writing—original draft. Faiqa Nadeem: review and editing. Muhammad Usman: review and editing. Muhammad Shahzaib: review and editing. Muneeb Ur Rahman: review and editing. Yang Liu: review and editing. Waheed Afzal: review and editing. Su Shiung Lam: review and editing. Zhiping Zhang: review and editing, funding acquisition.

Funding

This study was financially supported by the National Natural Science Foundation of China (52276183), the Natural Science Project of Henan Province (232300421063), and the Key Research and Development Program Project of Henan Province (251111110100).

Data availability

No data was used for the research in other studies described in the article.

Declarations

Competing interests

The authors declare that they have no known competing financial interests or personal relationships that could have appeared to influence the work reported in this paper.

Author details

[1]Collaborative Innovation Center of Biomass Energy, Henan Agricultural University, Zhengzhou 450002, China. [2]College of Landscape Architecture and Art, Henan Agricultural University, Zhengzhou 450002, China. [3]School of Engineering, University of Aberdeen, Aberdeen, Scotland, UK. [4]International Joint Laboratory of Biomass Energy and Nanomaterials in Henan Province, Henan Agricultural University, Zhengzhou 450002, China. [5]State Key Laboratory of High-Efficiency Production of Wheat-Maize Double Cropping, Henan Agricultural University, Zhengzhou 450002, China. [6]Higher Institution Centre of Excellence (HICoE), Institute of Tropical Aquaculture and Fisheries (AKUATROP), Universiti Malaysia Terengganu, Kuala Nerus, 21030 Kuala Terengganu, Terengganu, Malaysia. [7]University Centre for Research and Development, Department of Chemistry, Chandigarh University, Gharuan, Mohali, Punjab, India.

Received: 28 April 2025 Revised: 8 October 2025 Accepted: 19 October 2025
Published online: 22 February 2026

References

Atika, Dutta RK (2021) Oxygen-rich porous activated carbon from eucalyptus wood as an efficient supercapacitor electrode. Energy Technol 9(9):2100463

An T et al (2022) Deciphering physicochemical properties and enhanced microbial electron transfer capacity by magnetic biochar. Bioresour Technol 363:127894

Abbas S et al (2023) Tunable surface chemistry of carbon electrodes and the role of surface functionalities towards vanadium redox reactions. Appl Surf Sci 628:157331

Bu J et al (2021) Biochar boosts dark fermentative H2 production from sugarcane bagasse by selective enrichment/colonization of functional bacteria and enhancing extracellular electron transfer. Water Res 202:117440

Canto-Robertos M et al (2023) Inhibition of hydrogen production by endogenous microorganisms from food waste. Braz J Chem Eng 40(1):137–150

Di L et al (2022) Effect of nano-Fe3O4 biochar on anaerobic digestion of chicken manure under high ammonia nitrogen concentration. J Clean Prod 375:134107

Engliman NS et al (2017) Influence of iron (II) oxide nanoparticle on biohydrogen production in thermophilic mixed fermentation. Int J Hydrogen Energy 42(45):27482–27493

Eltaweil AS et al (2022) Novel biogenic synthesis of a Ag@ biochar nanocomposite as an antimicrobial agent and photocatalyst for methylene blue degradation. ACS Omega 7(9):8046–8059

Feng G et al (2023) Proteiniphilum and Methanothrix harundinacea became dominant acetate utilizers in a methanogenic reactor operated under strong ammonia stress. Front Microbiol 13:1098814

Gao Y et al (2022) A review on N-doped biochar for oxidative degradation of organic contaminants in wastewater by persulfate activation. Int J Environ Res Public Health 19(22):14805

Gao Y et al (2024) Understanding of the potential role of carbon dots in promoting interspecies electron transfer process in anaerobic co-digestion under magnetic field: focusing on methane and hydrogen production. Chem Eng J 489:151381

Gu Y et al (2023) Extracellular electron transfer and the conductivity in microbial aggregates during biochemical wastewater treatment: a bottom-up analysis of existing knowledge. Water Res 231:119630

Guo L et al (2023a) Peroxydisulfate activation using Fe, Co co-doped biochar and synergistic effects on tetracycline degradation. Chem Eng J 452:139381

Guo F et al (2023b) Biochar boosts nitrate removal in constructed wetlands for secondary effluent treatment: linking nitrate removal to the metabolic pathway of denitrification and biochar properties. Bioresour Technol 379:129000

Hamid Y et al (2022) Functionalized biochars: synthesis, characterization, and applications for removing trace elements from water. J Hazard Mater 437:129337

Hao J et al (2022) A stable Fe/Co bimetallic modified biochar for ofloxacin removal from water: adsorption behavior and mechanisms. RSC Adv 12(49):31650–31662

Hosny M, Fawzy M, Eltaweil AS (2022) Green synthesis of bimetallic Ag/ZnO@biohar nanocomposite for photocatalytic degradation of tetracycline, antibacterial and antioxidant activities. Sci Rep 12(1):7316

Houtman TA et al (2022) Gut microbiota and BMI throughout childhood: the role of firmicutes, bacteroidetes, and short-chain fatty acid producers. Sci Rep 12(1):3140

Ji J, Shen L (2024) Screening of enhanced biohydrogen production from anaerobic fermentation amended with nano-sized barium ferrite supported by aluminum oxide. Int J Hydrogen Energy 69:961–973

Jia Y et al (2021) Intra/extracellular electron transfer for aerobic denitrification mediated by in-situ biosynthesis palladium nanoparticles. Water Res 189:116612

Jiang N et al (2023) Iron cobalt-doped carbon nanofibers anode to simultaneously boost bioelectrocatalysis and direct electron transfer in microbial fuel cells: characterization, performance, and mechanism. Bioresour Technol 367:128230

Jiao P et al (2022) Effect of Clostridium butyricum supplementation on in vitro rumen fermentation and microbiota with high grain substrate varying with media pH levels. Front Microbiol 13:912042

Kayoumu M, Wang H, Duan G (2025) Interactions between microbial extracellular polymeric substances and biochar, and their potential applications: a review. Biochar 7(1):1–24

Li H et al (2020a) Role of acid gases in Hg0 removal from flue gas over a novel cobalt-containing biochar prepared from harvested cobalt-enriched phytoremediation plant. Fuel Process Technol 207:106478

Li W et al (2020b) Effects of biochar on ethanol-type and butyrate-type fermentative hydrogen productions. Bioresour Technol 306:123088

Li W et al (2025) Quantitative analysis of the mechanism of biochar in alleviating product inhibition in different fermentative hydrogen production processes. Biochar 7(1):1–14

Lin L et al (2024) Synthesis of Fe-doped sludge biochar from Fenton sludge for efficient activation of peroxymonosulfate in tetracycline hydrochloride degradation. J Environ Chem Eng 12(3):112590

Liu S et al (2023) Triggering photo fermentative biohydrogen production through NiFe2O4 photo nanocatalysts with various excitation sources. Bioresour Technol 1(385):129378

Liu Z et al (2023a) Porous Fe-doped graphitized biochar: an innovative approach for co-removing per-/polyfluoroalkyl substances with different chain lengths from natural waters and wastewater. Chem Eng J 476:146888

Liu S et al (2023b) Triggering photo fermentative biohydrogen production through NiFe2O4 photo nanocatalysts with various excitation sources. Bioresour Technol 385:129378

Liu J et al (2024) Enhanced activation of persulfate by bimetal and nitrogen co-doped biochar for efficient degradation of refractory organic contaminants: the role of the second metal. J Phys Chem Solids 193:112191

Ma H et al (2019) A simple route for hierarchically porous carbon derived from corn straw for supercapacitor application. J Renewable Sustainable Energy. https://doi.org/10.1063/1.5063676

Mei B-A et al (2018) Physical interpretations of electrochemical impedance spectroscopy of redox active electrodes for electrical energy storage. J Phys Chem C 122(43):24499–24511

Meng L et al (2023) Effects of different concentrations of biochar amendments and Pb toxicity on rhizosphere soil characteristics and bacterial community of red clover (Trifolium pretense L.). Front Plant Sci 14:1112002

Mikheeva ER et al (2022) Pretreatment in vortex layer apparatus boosts dark fermentative hydrogen production from cheese whey. Fermentation 8(12):674

Mostafa A et al (2016) Magnetite/graphene oxide nano-composite for enhancement of hydrogen production from gelatinaceous wastewater. Bioresour Technol 216:520–528

Nadeem F et al (2020) Defect engineering in SnO2 nanomaterials: pathway to enhance the biohydrogen production from agricultural residue of corn stover. Appl Mater Today 21:100850
Noguer MC et al (2022) Enhanced fermentative hydrogen production from food waste in continuous reactor after butyric acid treatment. Energies 15(11):4048
Rahman MU et al (2021) Solar driven photocatalytic degradation potential of novel graphitic carbon nitride based nano zero-valent iron doped bismuth ferrite ternary composite. Opt Mater 120:111408
Rahman MU et al (2024) Synergy of the heterojunction and defects engineering in Zr-doped TbFeO3@ g-C3N4 photo-nanocatalyst towards enhanced visible-light-driven antibiotics degradation and H2 production. Compos Part B Eng 287:111865
Rahman MU et al (2025) Enhanced charge transferring through defects-mediated metal-carbon nanocomposites for efficient dye degradation under visible light. J Water Process Eng 71:107225
Ramzan H et al (2019) Solar assisted cell wall disruption of indigenously isolated microalgae strains: process optimization. Mater Res Express 6(6):065506
Ramzan H et al (2023) Depolymerization of lignin: recent progress towards value-added chemicals and biohydrogen production. Bioresour Technol. https://doi.org/10.1016/j.biortech.2023.129492
Ramzan H et al (2024) Investigating the quantum size effects of multi-walled carbon nanotubes (MWCNTs) in photocatalytic fermentative biohydrogen production. J Clean Prod 449:141738
Ratheesh A et al (2024) Regulation of extracellular electron transfer by sustained existence of Fe^{2+}/Fe^{3+} redox couples on iron oxide-functionalized woody biochar anode surfaces in bioelectrochemical systems. Surf Interfaces 54:105114
Reddy A et al (2017) Genetic and functional drivers of diffuse large B cell lymphoma. Cell 171(2):481-494. e15
Ritzmann A.M. First principles insights into oxygen transport in solid oxide fuel cell cathode materials based on lanthanum strontium cobalt ferrite. 2016.
Roychowdhury S, Ghosh S (2024) State-of-the-art of biochar amended dark fermentative hydrogen production: a sustainable coupling of decarbonization pathways towards low carbon future. J Clean Prod. https://doi.org/10.1016/j.jclepro.2024.141208
Sathishkumar K, Li Y, Sanganyado E (2020) Electrochemical behavior of biochar and its effects on microbial nitrate reduction: role of extracellular polymeric substances in extracellular electron transfer. Chem Eng J 395:125077
Shahzaib M et al (2024) Maximizing the potential of biohydrogen production through cyclic photo fermentation: an approach towards zero waste. Energy Convers Manag 304:118234
Shu X et al (2022) Straw biochar at different pyrolysis temperatures passivates pyrite by promoting electron transfer from biochar to pyrite. Processes 10(10):2148
Simoes dos Reis G et al (2022) Facile synthesis of sustainable activated biochars with different pore structures as efficient additive-carbon-free anodes for lithium-and sodium-ion batteries. ACS Omega 7(46):42570–42581
Sridharan M et al (2021) Enhanced electrocatalytic activity of cobalt-doped ceria embedded on nitrogen, sulfur-doped reduced graphene oxide as an electrocatalyst for oxygen reduction reaction. Catalysts 12(1):6
Stojanov S, Berlec A, Štrukelj BJM (2020) The influence of probiotics on the firmicutes/bacteroidetes ratio in the treatment of obesity and inflammatory bowel disease. Microorganisms 8(11):1715
Sun L et al (2025) D-band center modulation of metallic co-incorporated Co7Fe3 alloy heterostructure for regulating polysulfides in highly efficient lithium-sulfur batteries. Adv Funct Mater 35(10):2416826
Sunyoto NM et al (2016) Effect of biochar addition on hydrogen and methane production in two-phase anaerobic digestion of aqueous carbohydrates food waste. Bioresour Technol 219:29–36
Suriyachai N et al (2020) Efficiency of catalytic liquid hot water pretreatment for conversion of corn stover to bioethanol. ACS Omega 5(46):29872–29881
Tahir N, Nadeem F, Zhang Q (2021) Optimisation of photo-fermentative biohydrogen production from corn stover through the synergetic effect of ultrafine grinding and SnO2 nanomaterials. J Clean Prod 328:129631
Tahir N et al (2022) Enhancing biohydrogen production from lignocellulosic biomass of Paulownia waste by charge facilitation in Zn doped SnO2 nanocatalysts. Bioresour Technol 355:127299
Tiang MF et al (2020) Recent advanced biotechnological strategies to enhance photo-fermentative biohydrogen production by purple non-sulphur bacteria: an overview. Int J Hydrogen Energy 45(24):13211–13230
Usman M et al (2024) Catalyzing the metabolism through CoFe2O4 magnetic photocatalyst for photo fermentative biohydrogen production: Selectivity and recyclability across diverse strains. Energy Convers Manage 319:118923
Usman M et al (2025) Manipulating electron shuttling in photo fermentative biohydrogen production from lignocellulosic biomass through engineered Z-scheme photo nanocatalysts. Chem Eng J 509:161047
Wang S, Wang J (2023) Bimetallic and nitrogen co-doped biochar for peroxymonosulfate (PMS) activation to degrade emerging contaminants. Sep Purif Technol 307:122807
Wang J, Yin YJIJoHE (2021) Clostridium species for fermentative hydrogen production: an overview. Int J Hydrogen Energy 46(70):34599–34625
Wang X et al (2019) 3D porous spherical sulfur/carbon cathode materials with in situ vapor-phase polymerized polypyrrole coating layer for high-performance lithium–sulfur batteries. ACS Sustain Chem Eng 7(20):17491–17499
Wang H et al (2020) Adsorption and Fenton-like removal of chelated nickel from Zn-Ni alloy electroplating wastewater using activated biochar composite derived from Taihu blue algae. Chem Eng J 379:122372
Wang H-R et al (2023a) A theoretical study of the effect and mechanism of FeN3-doped biochar for greenhouse gas mitigation. Biochar 5(1):23
Wang X et al (2023b) Electronic-state modulation of metallic co-assisted Co7Fe3 alloy heterostructure for highly efficient and stable overall water splitting. Adv Sci 10(22):2301961
Wang Z et al (2025) Insights into the interfacial dynamics and interaction mechanisms between phosphate-solubilizing bacteria and straw-derived biochar. Biochar 7(1):55
Wu Y et al (2024) Enhanced short-chain fatty acids production from food waste with magnetic biochar via anaerobic fermentation: linking interfacial, extracellular, and intracellular electron transfer. Chem Eng J 488:150853
Xia C et al (2022) A sulfur self-doped multifunctional biochar catalyst for overall water splitting and a supercapacitor from Camellia japonica flowers. Carbon Energy 4(4):491–505
Xiao K et al (2022) Magnetic bimetallic Fe, Ce-embedded N-enriched porous biochar for peroxymonosulfate activation in metronidazole degradation: applications, mechanism insight and toxicity evaluation. Chem Eng J 433:134387
Xu L et al (2020) Degradation of organic pollutants by Fe/N co-doped biochar via peroxymonosulfate activation: synthesis, performance, mechanism and its potential for practical application. Chem Eng J 400:125870
Yi W et al (2020) Modifying crystallinity, and thermo-optical characteristics of Paulownia biomass through ultrafine grinding and evaluation of biohydrogen production potential. J Clean Prod 269:122386
Yu Y et al (2025) Application of exogenous electron mediator in fermentation to enhance the production of value-added products. Appl Environ Microbiol. https://doi.org/10.1128/aem.00495-25
Zeng C et al (2024) Efficient degradation of sulfadiazine by UV-triggered electron transfer on oxalic acid-functionalized corn straw biochar for activating peroxyacetic acid: performance, mechanism, and theoretical calculation. Bioresour Technol 407:131103
Zhang Y et al (2022) Potential of biochar derived from three biomass wastes as an electrode catalyzing oxygen reduction reaction. Environ Pollut Bioavailab 34(1):42–50
Zhang M et al (2023) Preparation and adsorption properties of magnetic chitosan/sludge biochar composites for removal of Cu2+ ions. Sci Rep 13(1):20937
Zhu Z et al (2025) Biochar-mediated degradation of p-nitrophenol as influenced by species of Fe (III). Biochar 7(1):1–14